Atom Interferometry for Detection of Gravitational Waves

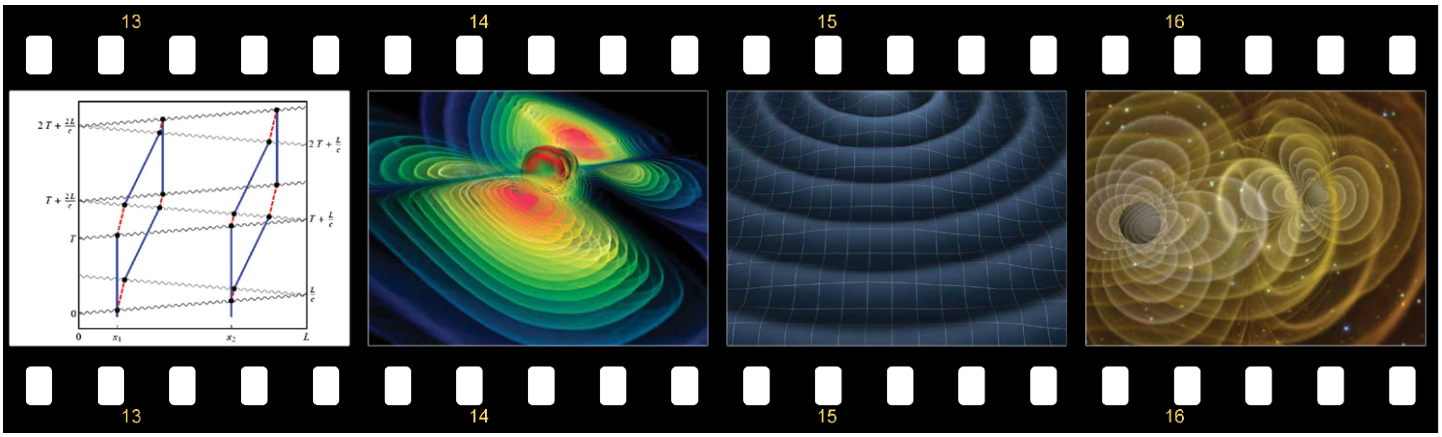

NIAC Phase 1 Final Report

Babak N. Saif • Jason Hogan • Mark A Kasevich

July 09, 2013

Table of Contents

1.Introduction 1-1
1.1 NAIC Phase 1 Study Concept 1-1
1.2 NAIC Phase 1 Project Summary 1-2

2. System Architectures. 1-3
2.1 Three Satellite Rb 1-3
2.2 Two Satellite Rb 1-4
2.3 Two Satellite Sr 1-4

3. Single Photon Gravitational Wave Detection 1-5
3.1 Introduction 1-5
3.2 A New Type of Atom Interferometer 1-6
3.3 A Differential Measurement 1-7
3.4 Backgrounds 1-8
3.5 Atomic Implementation 1-9
3.6 Discussion 1-9

4. Point Source Interferometry 1-10

5. Enhanced Atom Interferometer Readout through the Application of Phase Shear 1-14

Appendix A 1-20

Bibliography 1-37

1. Introduction

Gravitational wave (GW) detection promises to open an exciting new observational frontier in astronomy and cosmology. In contrast to light, gravitational waves are generated by moving masses – rather than electric charges – which means that they can tell us about objects that are difficult to observe optically. For example, binary black hole systems (which might not emit much light) can be an ample source of gravitational radiation. In addition to providing insights into astrophysics, observations of such extreme systems test general relativity and might influence our understanding of gravity. Cosmologically, since GWs are poorly screened by concentrations of matter and charge, they can see places other telescopes cannot – even to the earliest times in the universe, beyond the surface of last scattering.

In principle, GWs can be observed by monitoring the distance between two "test masses" separated by some large baseline, but direct detection has remained elusive because GWs are incredibly weak. Existing detectors such as LIGO (Laser Interferometer Gravitational-Wave Observatory) use laser light to simultaneously measure the lengths of two baselines pointing in different directions, usually at right angles. This trick exploits the fact that GWs are quadrupolar: when one baseline direction is stretched, the perpendicular baseline is compressed. By combining the signals from its perpendicular baselines, LIGO and other interferometric detectors cancel laser noise that would otherwise spoil the measurement, while still maintaining sensitivity to the anisotropic stretch of GWs.

1.1 NIAC Phase 1 Study Concept

The concept described in this report is a fundamentally new GW detection method based on atom interferometry.[1, 2, 3] Critically, we suggest using freely-falling atoms as the "test masses" in place of the macroscopic references currently in use or envisioned (e.g., LIGO's mirrors). This potentially avoids several limitations of optical detectors and lets us exploit the powerful techniques that have recently led to dramatic improvements in atomic timekeeping[4] and inertial measurement.[5, 6] An Atomic Gravitational wave Interferometric Sensor (AGIS) could operate in frequency ranges that are conventionally inaccessible, and could reach the same level of GW sensitivity as other proposed detectors, but with a dramatic reduction in the length of the required baseline. Tantalizingly, an AGIS detector would also circumvent the need for multiple baselines, opening up a new "single-arm" detector design paradigm that may have advantages in cost and flexibility.

The proposed atom-based GW antenna (see Fig. 1.1(a)) is similar to well-established atom interferometric gravity gradiometers.[7] Dilute clouds of ultracold atoms at either end of the baseline act as inertial test masses, and laser light propagates between the atoms. To implement atom interferometry, the lasers from sources S_1 and S_2 are briefly pulsed a number of times during each measurement cycle. The paths of these light pulses appear as wavy lines in Fig. 1.1(b). The two diamond-shaped loops represent the atom interferometers. Interaction with a light pulse transfers momentum lk to the atom and toggles the atomic state between the ground and the excited states. As a result, the light pulses act as beamsplitters and mirrors for the atom de Broglie waves, dividing them into a quantum superposition of two paths and even-

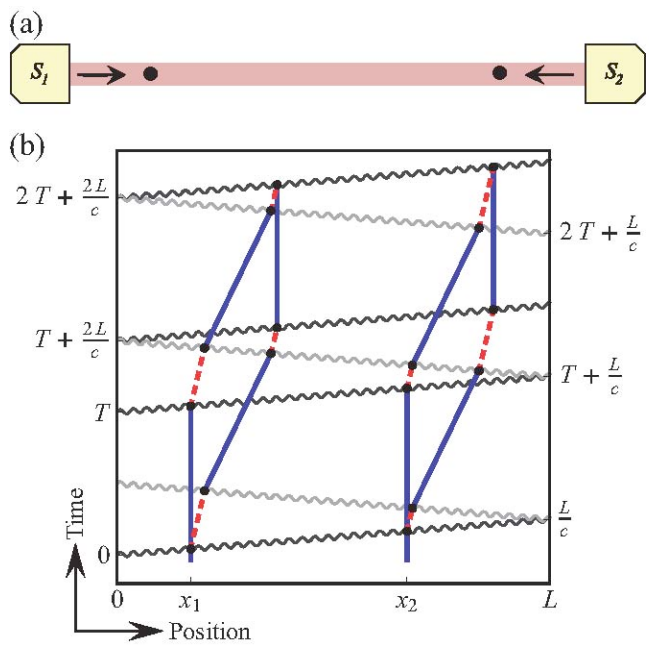

Figure 1-1: Gravitational wave detection using atoms. **(a)** Dilute clouds of atoms (black circles) at either end of a long baseline act as inertial test masses. Laser light (red) propagates between the atoms from sources S_1 and S_2. **(b)** Space-time diagram of the trajectories of both atom interferometers, showing the ground (blue) and excited (red dashed) atomic states. Short laser pulses (wavy lines) traveling from alternating sides of the baseline are used to divide, redirect, and recombine the atom de Broglie waves, yielding atom interference patterns that are highly sensitive to any modulation of the light travel time caused by gravitational radiation. The spatial extent of the atom interferometers relative to the baseline has been exaggerated..

tually recombining them. Similar to an atomic clock, the phase shift recorded by each atom interferometer depends on the time spent in the excited state, which here is directly tied to the light travel time (L/c) across the baseline. GWs can be detected because they modulate the light travel time.

An essential feature of the AGIS detector is that it incorporates a differential measurement between two atom interferometers to cancel laser frequency noise that would otherwise overwhelm the GW signal. Since each laser pulse interacts with both atom interferometers, the imprinted laser noise is a common mode, and taking the differential phase $\Delta\phi = \phi 1 - \phi 2$ between the two interferometers eliminates this noise while retaining the GW signal. This differential measurement protocol enables an atom-based detector to use only a single arm, avoiding the need for perpendicular baselines.

Figure 1.2 shows the GW strain sensitivities possible for a terrestrial and a satellite AGIS detector compared to LIGO and the proposed space-based LISA (Laser Interferometer Space Antenna). Note that the intrinsic seismic isolation provided by freely-falling atoms would allow for substantially lower frequency detection on Earth than LIGO. In space, an AGIS detector could achieve sensitivity comparable to LISA while using a 1000 times shorter baseline. Additionally, AGIS is insensitive to many mechanical noise sources,[1] thus dramatically reducing satellite acceleration noise requirements – a key technical challenge faced by LISA.

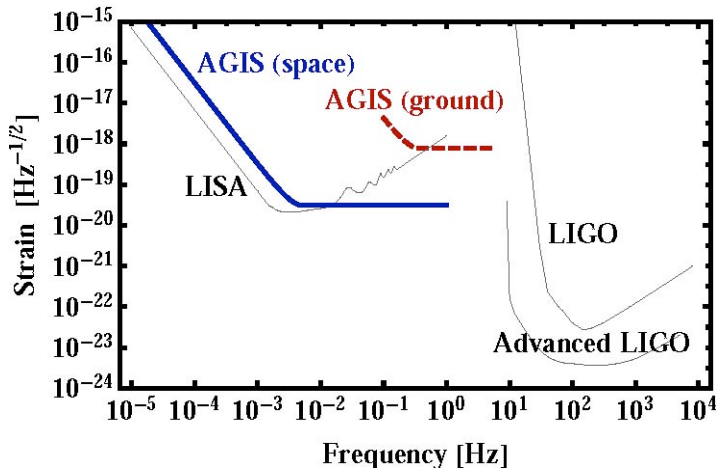

Figure 1-2: Example strain sensitivity curves for proposed terrestrial (red dashed) and satellite (blue solid) atom GW detectors. Terrestrial parameters: $L = 4$ km, 1000$\hbar k$ atom optics and $T = 1.4$ s; Satellite parameters: $L = 10^3$ km, 100$\hbar k$ atom optics (recently demonstrated[8]) and $T = 100$ s. Both assume 10^8 atoms/s shot-noise limited phase detection. LIGO and LISA sensitivity curves (gray thin) are shown for reference.

1.2 NIAC Phase 1 Project Summary

This report presents the results of the 2012-2013 NASA Institute for Advanced Concepts (NIAC) Phase 1 "Atom Interferometry for Detection of Gravitational Waves" project. The origin of this GW detection concept using atoms can be traced to theoretical work that first appeared in 2008 [2] and also to a satellite mission-focused followup study that was done in 2011 [3]. The goal of the current project was to explore both theoretical and technical issues surrounding the implementation of this idea, as well as to begin performing proof-of-concept experiments to validate critical aspects of the proposal.

The top level trade space for the detector design is driven by the strategy employed to mitigate laser frequency noise, which, if uncontrolled, can mask GW signatures. One of the advantages of the atom interferometric approach is the possibility of single baseline detection (Fig. 1.1), even in the presence of laser noise. This is enabled by the differential measurement between the two ensembles of atoms, which can result in substantial laser noise suppression. The details of this suppression depend on the atomic physics techniques used to implement the atom interferometry. Specifically, we considered the effect on noise suppression that results from using traditional two-photon Raman transitions (with alkali atoms) and also single-photon transitions (with alkaline earth-like atoms).

The interferometers shown in Fig 1.1(b) take advantage of single-photon transitions (as opposed to traditional Raman transitions) because using light pulses from one direction at a time allows for near perfect common-mode cancellation of laser phase noise, even for long baselines.[1] This calls for the use of atomic transitions with an (ideally large) optical energy level difference with a long (> 1 s) lifetime, such as high- transitions routinely used for optical atomic clocks in species like Sr, Ca and Yb. Notably, large momentum transfer (LMT) atom optics[8] – and the sensitivity enhancement they confer – can still be realized by simply adding additional pairs of alternating pulses to each beamsplitter process.[1] Section 3 reports on the theoretical work we performed to justify this GW detection protocol using single-photon transitions. This approach represents a new method for GW detection

using atoms that is distinct from the original proposal from 2008.

At the system level, we evaluated three architectures, each of which implements a different solution to the laser frequency noise issue. The first two designs are based on two-photon Raman transitions with Rb atoms. One of these is a three-satellite, multiple baseline design while the other is a two-satellite, single baseline design. The third proposal is a two-satellite, single baseline design that uses single-photon transitions with Sr atoms. These three architectures are described in more detail in Section 2.

There are a number of known technical issues that we have started to address using ground-based experiments. These issues include atom technology development needs such as, for example, lower ensemble temperature requirements and large momentum transfer (LMT) atom optics. To this end, we have built a 10-meter scale atom drop tower[9, 10] where we can perform proof-of-principle demonstrations of the proposed AGIS detector in an environment that permits more than 2.5 seconds of free-fall time. This facility allows for demonstration of atom interferometry with long interrogation time (seconds) and large atom wavepacket separation (meters), which is the regime required for GW detection at scientifically interesting levels.

Sections 4 and 5 describe the results of these experiments. Section 4 describes the demonstration of an atom interferometer at high contrast with a record interrogation time of $2T$ =2.3 seconds, as well as a new technique for evaluating and controlling velocity dependent systematic phase shifts that typically cause inhomogeneous broadening that reduces interferometer contrast. Section 5 is a discussion of a new interferometer phase readout procedure that we developed. This new technique, called Phase Shear Readout (PSR) allows the phase and contrast of the interferometer to be measured with a single shot. PSR has the potential to offer a dramatic reduction in a variety of noise requirements for the GW detector, including satellite rotation stability and optical wavefront aberrations.

2. System Architectures

We explored three system architectures to address laser phase noise. One of the central design factors in this analysis is the atom optics process used to implement the atom interferometers. As discussed in detail in Section 3, atom optics based on single-photon transitions can have superior laser phase noise rejection than two-photon atom optics. However, the choice of atom optics is tied to the choice of atomic species. Alkaline-earth like atoms possess narrow optical transitions with very long lifetime that are compatible with single-photon atom optics. Alkali atoms, on the other hand, are traditionally manipulated using two-photon atomic optics (Raman or Bragg transitions) to avoid decoherence from the decay of the generally short-lived excited states of available optical transitions.

Here we consider two example atomic species as representative of these categories: Rb for the two-photon case and Sr for the single-photon case. We emphasize that the choice of these atoms for this discussion should not be taken to mean that we have ruled out other species. In fact there are a number of promising choices in each category that present a variety advantages that require careful consideration. Rather, we frame this discussion in terms of Rb and Sr because they are well studied in the atom interferometry and atomic clock communities, and because they serve as specific, viable solutions technologically. Nevertheless, the selection of the optimal atom remains a subject of ongoing investigation.

2.1 Three Satellite Rb

The first system architecture uses Rb atoms with interferometry based on two-photon atom optics. To reject residual laser frequency noise, this configuration uses a conventional multiple baseline arrangement. The baselines are established between a constellation of three satellites, with laser light connecting each pair of satellites to form three baselines in the shape of a triangle. Each baseline contains two atom interferometers, one at each end, in a manner identical to Fig. 1.1. In a way analogous to LISA, laser phase noise is shared among the baselines and can be rejected as a common mode.

The system level diagram for this architecture is shown in Fig. 2.1. Atom interferometry is implemented between each pair of satellites by means of laser light that originates in each satellite and that is directed towards the opposing satellites. Within each satellite, light from a low noise master laser oscillator is split into two paths that are ultimately used to implement the atom interferometry in the two baselines that connect to the satellite. This master light is amplified and then delivered to the interferometer regions by a pair of telescopes that point towards the other satellites. The design is such that the phase noise present on the master laser is delivered to both baselines, so a comparison of the signals derived from these baselines can be used to reject the common noise.

The satellites also include onboard accelerometers to address the effect of satellite acceleration noise

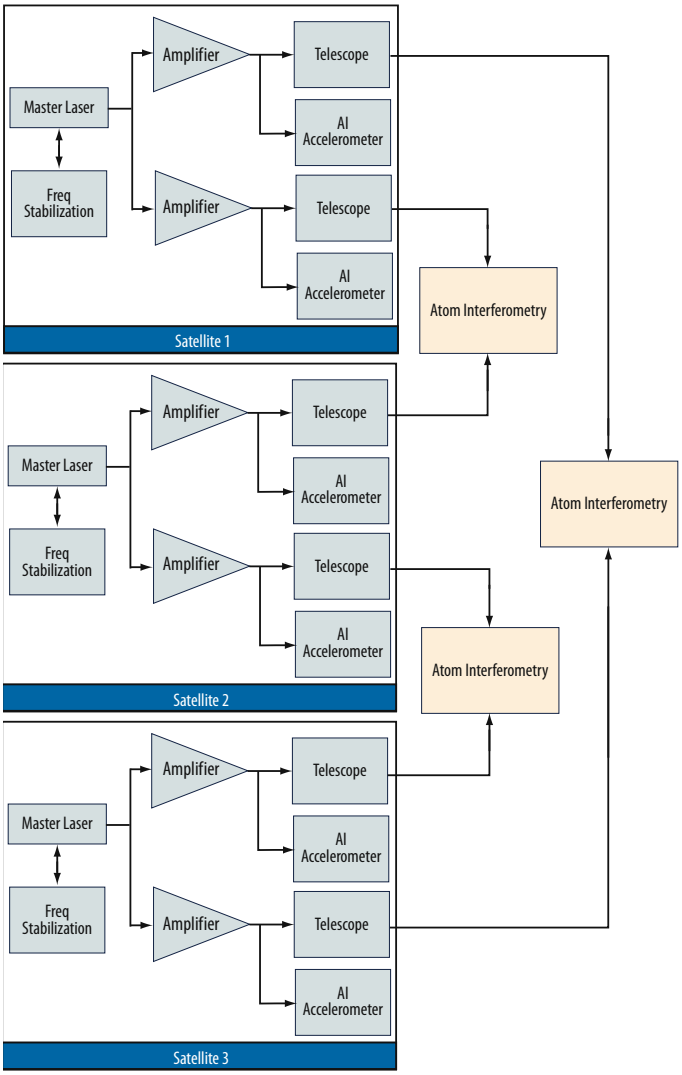

Figure 2-1: System diagram for three satellite Rb detector.

on the detector. Vibration of the satellite leads to frequency noise on the interferometer laser beams because of the Doppler effect. By measuring the instantaneous local acceleration of the satellite, it is possible to account for this noise effect if the accelerometer is sufficiently precise. Here we call for atom interferometric (AI) accelerometers (distinct from the atom interferometers used to detect the GW signal).

AI accelerometers can provide sufficient precision and can be accommodated using the same infrastructure already in place to implement the main atom interferometers used to detect the GW signal.

2.2 Two Satellite Rb

The second architecture is also based on Rb interferometry, but here in a single-baseline, two satellite arrangement. Reducing the design to a single baseline is motivated by a desire to reduce cost and system-level risk associated with formation flying of three satellites. However, without the benefit of multiple baselines to help reject laser noise, this design requires a new approach to laser noise mitigation. The solution here is to measure the instantaneous phase noise of the laser with a local phase meter. If the phase meter has sufficient precision, then the phase measurements can be used to reject the phase noise from the GW data stream (the noise can be subtracted from the signal channel).

The phase meter consists of a high stability atomic frequency reference and an optical frequency comb (see Fig. 2.2). The frequency reference is based on the narrow clock transition in (for example) atomic strontium ($5s^2\,{}^1S_0 \rightarrow 5s5p\,{}^3P_0$). This atomic transition can serve as a phase reference because the transition is insensitive to environmental perturbations and, in part since it is an optical transition, it can be interrogated with sufficient precision.

When performing Rb interferometry to detect GWs, each time the interferometer laser is pulsed it will imprint its phase noise on the Rb atoms, contaminating the GW data with this noise. Once again, the protocol of this design is to measure the phase of the interferometer laser each time it is pulsed by comparing it to the Sr phase reference. Since the Sr reference transition has a different wavelength than the Rb interferometer laser, this comparison must be facilitated by an optical frequency comb. The frequency comb can be used to transfer the stability of the Sr reference to a wavelength near the Rb interferometer laser so that the interferometer laser phase can be measured.

As in the three satellite Rb design, this two satellite architecture is also sensitive to satellite acceleration noise, which results in laser frequency noise via the Doppler effect. This additional phase noise cannot be measured by the local Sr phase reference. As before, this noise is addressed by measuring the acceleration of the satellite using an AI accelerometer on each satellite.

2.3 Two Satellite Sr

The third architecture is a single-baseline, two satellite arrangement using interferometry based on single-photon transitions in Sr. The phase noise immunity offered by the single-photon transi-

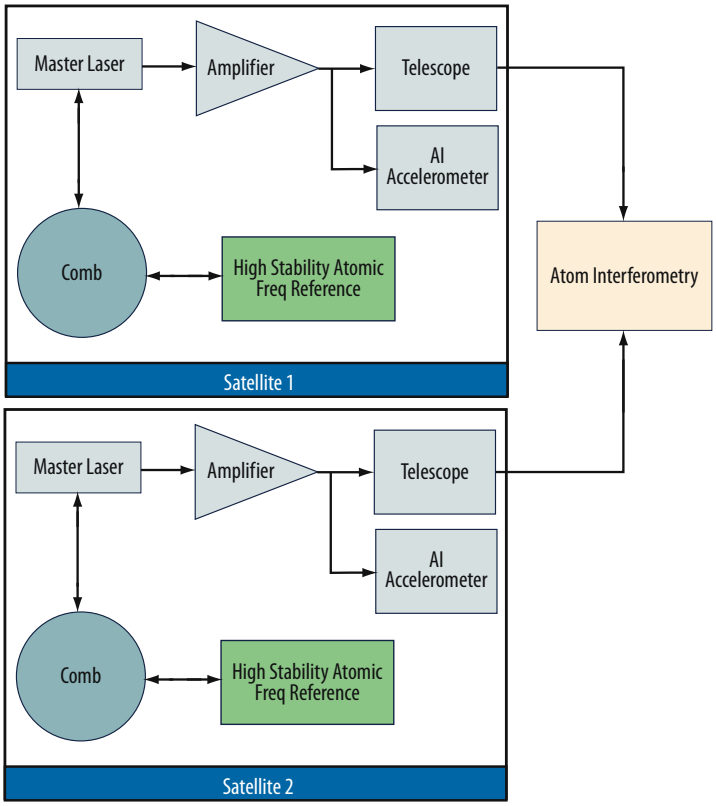

Figure 2-2: System diagram for two satellite Rb detector. The atomic frequency reference is realized using the optical clock transition in atomic Sr.

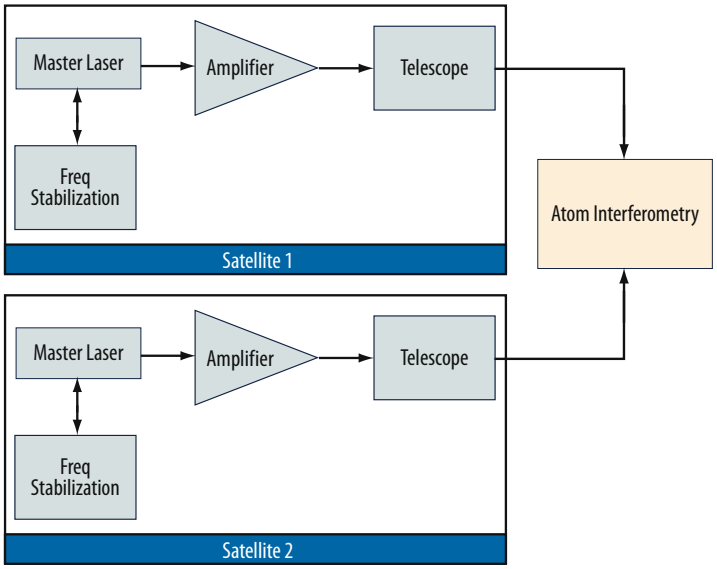

Figure 2-3: System diagram for two satellite Sr detector.

tion technique (see Section 3) results in a substantial simplification of the overall design, because any noise on the laser is naturally rejected in the differential measurement between the two interferometers along the single baseline. Each satellite contains a master laser that is stabilized to the Sr transition. This light is amplified and delivered by a telescope to the atom interferometer region between the two satellites (see Fig. 2.3).

Once again, satellite vibration noise gets imprinted on the laser via the Doppler shift. However, unlike the previous two designs, this noise is largely rejected by the differential measurement between the Sr interferometers, and so local accelerometers are not required.

Although the use of single-photon atom optics leads to a substantial suppression of the influence of laser and other noise sources, these effects are not perfectly rejected if there is a nonzero velocity between the atom ensembles on opposite sides of the baseline. The residual, leading order susceptibility in this design to kinematic disturbances (such as satellite acceleration noise) and laser noise is discussed in Section 3.4.

3. Single photon gravitational wave detection

3.1 Introduction

The observation of gravitational waves will open a new spectrum in which to view the universe [11]. Existing detection strategies are based on long-baseline optical interferometry [12, 13], where gravitational waves induce time-varying phase shifts in the optical paths. Spurious phase shifts arising from laser frequency and phase noise are suppressed through multi-arm configurations which exploit the quadrupolar nature of gravitational radiation to separate gravitational wave induced phase shifts from those arising from laser noise. In the absence of such noise, a single baseline optical interferometer, *e.g.* a Fabry-Perot interferometer, would suffice for gravitational wave detection. In these detectors, stringent constraints are also placed on the mechanical motion of the interferometer optics in order to avoid optical path length fluctuations which would otherwise obscure the gravitational wave signals.

We propose a new approach, based on recent advances in optical frequency control and atom interferometry, which directly avoids laser frequency noise and naturally mitigates mechanical noise sources. The approach draws on the development of light-pulse gravity gradiometers, where Doppler-sensitive two-photon optical transitions are used to measure the differential acceleration of two spatially separated, free-falling, laser cooled atomic ensembles [7, 14, 15]. For these sensors, the optical interrogation is configured so that the same laser beams interrogate both ensembles of atoms along a common line-of-sight. This significantly suppresses laser frequency noise, but does not remove it completely due to the time delay introduced by the travel time of the light between ensembles and the need for each of the two counter-propagating laser beams to temporally overlap (in order to drive the two-photon transitions) [14, 16]. For shorter baseline instruments (*e.g.* 1 m gravity gradiometers), this noise source is relatively benign. For longer-baseline gravitational wave detectors (*e.g.* 10 km -1000 km baseline AGIS proposals described in Refs. [2, 3]), it becomes a dominant noise source [17]. It also places stringent limits on knowledge of residual accelerations of the laser platform, which manifest themselves as Doppler shifts on the frequency of the light in the inertial frame of the atoms.

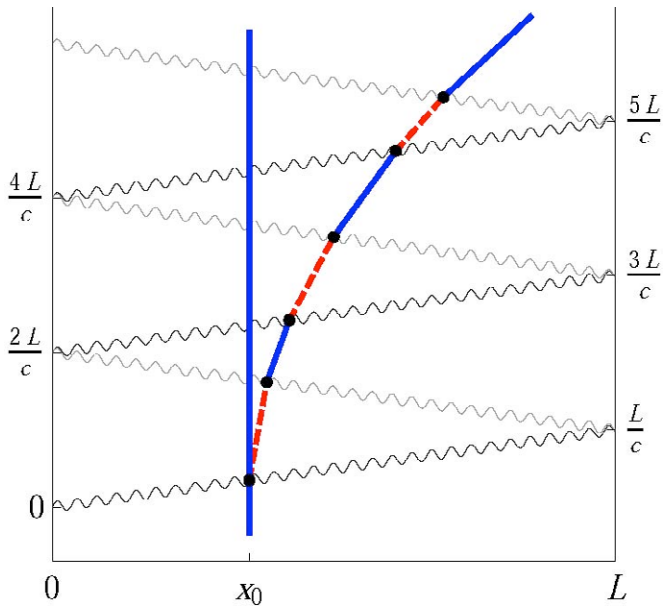

Figure 3-1: A space-time diagram of our proposed LMT beamsplitter with $N = 3$. The solid (blue) lines indicate the motion of an atom in the ground state, the dashed (red) lines indicate the atom in the excited state. Light pulses from the primary and secondary lasers are incident from the left (dark gray) and the right (light gray) respectively. Dots indicate the vertices at which the laser interacts with the atom.

Laser noise would nearly disappear if the atomic transitions were driven with a single laser pulse since the laser frequency noise in each pulse would be common to both atom interferometers and would cancel in the differential measurement. This follows from the relativistic formulation of atom interferometry in Ref. [18] since the laser phase of a pulse is set when the pulse is emitted and does not change as it propagates along the null geodesic connecting the laser to the atoms. We propose a laser excitation protocol which is based solely on single photon transitions in order to exploit this noise immunity and which is capable of achieving scientifically interesting strain sensitivities. In an optical interferometric gravitational wave detector, the relative phases of the interfering optical fields serve as proxies for the propagation time of the light along the interferometer arms. In the proposed approach, gravitational waves are instead sensed by direct measurement of the time intervals between optical pulses, as registered by atomic transitions which serve as high stability oscillators.

3.2 A New Type of Atom Interferometer

Due to atomic momentum recoil in the absorption and stimulated emission of photons during optical interactions, the proposed pulse sequence, detailed below, can be understood as a variant of a light-pulse de Broglie wave interferometer in a Mach-Zender configuration [19, 20, 21]. A prototypical excitation sequence can be described as a combination of beamsplitter and mirror segments.

For the beamsplitter, the lasers are pulsed as in Fig. 3.1. The primary laser is taken to be at $x = 0$, the left side of the figure, the secondary laser is taken at $x = L$, the right side of the figure. The atom begins at $x = x_0$ in the ground state. The initial pulse at time $t = 0$ isa $\pi/2$ pulse which splits the atom's wavefunction in two (for simplicity, we neglect spontaneous emission from the excited state). Some time after this reaches x = L,a π pulse is fired from the secondary laser which is Doppler tuned to interact only with the half of the atomic wavefunction which was originally excited. In Fig. 3.1 the second pulse is taken to leave at the time L/c when the first pulse arrives at $x = L$, but in fact it is only necessary that the second pulse leaves after this time. After the initial pair of pulses, to make a large momentum transfer (LMT) beamsplitter $N - 1$ more pairs of π pulses are sent, each pair having the first pulse from

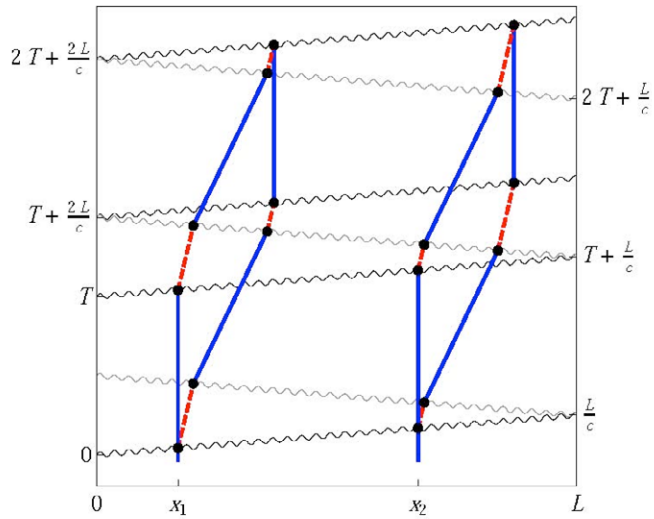

Figure 3-2: A space-time diagram of the proposed configuration of a differential measurement between two atom interferometers beginning at positions x_1 and x_2. The lines are as in Fig. 3.1. For clarity the beamsplitters shown are not LMT, *i.e.* here $N = 1$.

the primary laser and the second from the secondary laser. The frequency of these pulses are tuned so they interact only with the faster half of the atom. This is shown in Fig. 3.1 for $N = 3$. This leaves half of the atom's wavefunction in the ground state with unchanged momentum (the left solid line in Fig. 3.1) and gives a momentum of $2N\hbar k$ to the other half of the atom, where k is the wavevector of each pulse. This sequence makes an LMT beamsplitter using only single-photon atomic transitions. Note that according to the standard rules which govern the laser/atom interactions, the phase of the laser field is read into the atomic coherence during each of the atomic transitions.

The basic mirror sequence is three π pulses, alternately from the primary and secondary lasers as shown in the middle of Fig. 3.2. In general, there are several ways to realize this sequence. It can begin either from the primary laser (as shown in Fig. 3.2) or from the secondary laser. The pulses are tuned using a modulator on an extremely stable laser to interact only with certain halves of the atom, as indicated by the dots in Fig. 3.2. To make the entire LMT mirror pulse, $N - 1$ pairs of laser pulses are added before the basic mirror sequence to slow down the fast half of the atom, the exact opposite of the initial beamsplitter. Similarly $N - 1$ pairs are added after the basic mirror sequence to accelerate the other half of the atom. This reverses the momenta of the two incoming halves of the atom's wavefunction. The slow half gets a momentum kick of $2N\hbar k$, the fast half loses $2N\hbar k$.

Using a beamsplitter-mirror-beamsplitter sequence allows the atom interferometer to close, so that the two halves of the atom's wavefunction overlap at and can be interfered by the final beamsplitter. The phase difference is read out by measuring the atom populations in the interferometer output ports. The mirror pulse is started at time $t = T$ and the final beamsplitter is started at time $t = 2T + \frac{L}{c}$. This is shown in each half of Fig. 3.2.

This type of atom interferometer acts effectively as an accelerometer. If the atom does not accelerate, the time spent in the excited state is the same for each half of the atom's wavefunction and there is no phase difference. However if the atom accelerates, this time is not the same. Since the atom accumulates phase faster in the excited state, this gives rise to a phase shift proportionally to the acceleration. Interestingly, the phase shift is read in to the atom during the relatively short beamsplitter and mirror sequences themselves, not during the large interrogation time ~ T between them. Nevertheless, these phase shifts scale proportionally to T since they depend on the change in the light travel time across the baseline between the beamsplitter and mirror sequences. The phase shift (or sensitivity) of this type of atom interferometer also scales with N. The leading order phase shift in a local gravitational field is $\sim N\omega_a g T^2/c$ where ω_a is the atomic energy level difference and g is the acceleration due to gravity (here assumed constant in space and time). The phase shift due to a gravitational wave is approximately the same with g replaced by the acceleration caused by the gravitational wave. Intuitively the factor of N arises because the signal comes from the extra time spent in the excited state [the dashed (red) lines in Fig. 3.2)] which increases linearly with N.

These leading order phase shifts are proportional to the atomic energy difference ω_a, not to the laser frequency $\omega = kc$. This is a known difference between atom optics based on two-photon Raman or Bragg transition (where $\omega_a \ll 1$ eV), and a single-photon transition (where ω_a is large, ~ 1 eV) [18]. In practice the laser must be tuned so that ω is close to ω_a in order to drive the atomic transition.

3.3 A Differential Measurement

A single interferometer of the type described above will have laser noise, but this can be removed by a differential measurement between two such interferometers (similar to the scheme proposed in

Refs. [22, 2, 3]). The primary and secondary lasers are separated by a large distance L, with atom interferometers operated near them. The atom clouds are initially prepared as described in [2]. These two widely separated atom interferometers are run using common laser beams (see Fig. 3.2) and their differential phase shifts measured. Importantly, for any given interogation, the same laser beam drives both interferometers. For example, the pulse from the primary laser at time $t = 0$ triggers the initial beamsplitter for *both* interferometers and the pulse from the secondary laser at time $t = L/c$ completes this beamsplitter, again for both interferometers. We will show that the differential phase shift between these interferometers contains a gravitational wave signal proportional to the distance between them. However, since the *same* laser pulse operates *both* interferometers, the differential signal is largely immune to laser frequency noise. This idea has some similar features to the proposal described in Ref. [23], where a single laser only is used to interrogate two spatially separated atomic ensembles.

To see the effect of a gravitational wave on the differential phase between the two interferometers, assume that one interferometer is at $\chi_1 = 0$ in Fig. 3.2 while the other is at $\chi_2 = L$ and $T \gg L/c$. In the absence of a gravitational wave, each arm spends a time L/c in the excited state leading to a null result in each interferometer. Note though that the arms of the interferometer at χ_1 spend time L/c in the excited state in the beginning and the middle of the interferometer, while the arms of the interferometer at χ_2 spend time L/c in the excited state in the middle and end (see dashed lines in Figure 3.2). In the presence of a gravitational wave of strain h and frequency ω, the distance between the atom interferometers oscillates in time. This affects the laser pulse travel time which in turn affects the relative time spent by each atom interferometer arm in the excited state (see Fig. 3.2). When $T \sim 1/\omega$ the distance changes by $\sim h L$ in time T (assuming $\omega L/c \ll 1$). Hence, the two interferometers spend a slightly different amount of time $\sim h L/c$ in the excited state. This leads to a differential phase shift between the interferometers of $\sim \omega_a h L/c$. For an LMT sequence with N pulses, the phase shift is enhanced by N since it adds during each pulse. A fully relativistic calculation following the formalism of [18] yields the differential phase shift to be

$$\Delta\phi = \frac{4N\omega_a h}{c}(x_1 - x_2)\sin^2\left(\frac{\omega T}{2}\right)\sin(\phi_0 + \omega T) \tag{3.1}$$

proportional to the baseline $\chi_1 - \chi_2 \approx L$. ϕ_0 in this expression is the phase of the gravitational wave at the start of the experiment, whose change ($\phi_0 = \omega t_0$) causes a time dependent phase shift in the experiment. This phase shift is measured by operating successive interferometers at a rate higher than the Nyquist frequency necessary to measure the signal [22, 2, 3].

The gravitational wave signal is due to the oscillation of the laser ranging distance between the two interferometers. The atoms effectively measure the light travel time across the baseline. Thus, the lasers do not serve as a clock and so do not need a highly stable phase evolution. Remarkably, only the constancy of the speed of light across the baseline is relevant. This is an important change from all other interferometric gravitational wave detection schemes, where the laser serves the role of a phase reference, thus requiring additional noise mitigation strategies (*e.g.* additional measurement baselines).

3.4 Backgrounds

We will now discuss possible noise sources for the proposed scheme. We distinguish between two classes of noise: intrinsic laser noise and kinematic noise. Intrinsic laser noise refers to jitters in the phase and frequency of the laser while kinematic noise is caused by the acceleration noise of the laser platform and jitter in the timing between the interferometer pulses. The phase of a laser pulse does not evolve during its propagation in vacuum from the laser to the location of the atom[1]. Hence the atoms record the phase of the laser which exists at the emission time of the pulse. Since both interferometers are operated by the same laser pulses, the intrinsic laser noise read by both interferometers is identical and will cancel in the differential phase. The kinematic sources of noise affect both the imprinted laser phase and the amount of time spent by the arms of the interferometer in the excited state. Again, the noise from the imprinted laser phase will completely cancel in the differential measurement since the same laser pulses are used to drive both interferometers. However, any kinematic difference such as a relative velocity $\Delta\upsilon$ between the two interferometers will result in differences in the time spent in the excited state between the two interferometers, leading to a differential phase shift suppressed by $\frac{\Delta\upsilon}{c}$.

1 Noise can arise from fluctuations in the refractive index n of the medium of light propagation. For space-based detectors, fluctuations δn_p in the solar plasma density n_p give an effective strain of h ~ (n−1)

	Phase Shift	Control Required	Freq. Dependence
1.	$N\frac{\Delta v}{c}\frac{\omega_a}{c}T^2\delta a$	$\delta a \lesssim 10^{-8} g/\sqrt{\text{Hz}}$	$\times\left(\frac{\omega/2\pi}{10\ \text{mHz}}\right)^2$
2.	$N\frac{\Delta v}{c}\omega_a\delta T$	$\delta T \lesssim 10^{-12}$ s	$\times\left(\frac{\omega/2\pi}{10\ \text{mHz}}\right)^0$
3.	$N\Delta v\,\delta k\,\Delta\tau$	$c\delta k/2\pi \lesssim 10^2$ kHz$/\sqrt{\text{Hz}}$	$\times\left(\frac{\omega/2\pi}{10\ \text{mHz}}\right)^0$
4.	$N^2\frac{\Delta v}{c}\frac{\hbar}{m}\frac{\omega_a}{c}T\delta k$	$c\delta k/2\pi \lesssim$ GHz$/\sqrt{\text{Hz}}$	$\times\left(\frac{\omega/2\pi}{10\ \text{mHz}}\right)$

Table 3-1: A list of dominant noise terms, the control required to achieve a sensitvity of $h \sim \frac{10^{-20}}{\sqrt{\text{Hz}}}$, and the scaling of this requirement with frequency ω We assume an example satellite-based configuration with a baseline of 1000 km so the relative velocity between the two atom interferometers is $\Delta v \lesssim 1\frac{\text{cm}}{\text{s}}$ (see e.g. [25]). We take $T \approx 50$ s, $\Delta\tau \approx 10$ ms and $N \approx 300$. All requirements are at a frequency of 10 mHz. These requirements are several orders fo magnitude easier to achieve tha the state-of-the-art.

Following the formalism of [18] we calculate the differential phase shifts (shown in Table 3.1) caused by platform acceleration noise δa, jitter δT in the time between pulses, and laser frequency jitter δk[2]. Each of the resulting error terms has its origin only in an initial velocity mismatch $\Delta\upsilon$ between the two atomic sources, and is thus suppressed by $\Delta\upsilon/c <\sim 3 \times 10^{-11}$. Also included in the analysis are corrections related to the finite duration $\Delta\tau$ of the laser pulses [26]. The frequency dependence is estimated from the condition $\omega T \sim \pi$ [see Eq. (3.1)], which determines the low-frequency corner of the antenna response [2]. We note that this differential measurement scheme does not remove noise from wavefront aberration [27, 28], since after diffraction aberrations are not generally common to both interferometers. However, straightforward noise mitigation schemes suggested in [29, 3] can successfully address these issues. Finally, ellipse specific methods [15, 30, 31] can be used to extract the differential phase shift in the presence of the common-mode laser phase noise.

3.5 Atomic Implementation

The proposed LMT scheme requires a two-level system with a large (optical) energy difference ω_a and a long excited state lifetime τ . To maintain interferometer contrast, the total time $\sim NL/c$ that the atom spends in the excited state during the interferometer sequence cannot exceed τ. Taking $\tau = NL/c$ as an upper bound, we can write the peak phase sensitivity in Eq. 3.1 in terms of the quality factor $Q = \omega_a\tau$ of a given atomic transition, resulting in $\Delta\phi_{max} = 4\omega_a(NL/c)h = 4Qh$. This suggests that the same atoms typically selected for optical clocks because of their high Q transitions are also appropriate for this proposal. An optical transition with mHz linewidth has $Q > 10^{17}$ which could support a strain sensitivity $h < 10^{-21}/\sqrt{\text{Hz}}$ assuming atom shot-noise limited phase noise $\delta\varphi = 10^{-4}/\sqrt{\text{Hz}}$. For gravitational wave detection with $N = 300$ and baseline $L = 1000$ km we have $2NL/c = 2$ s, requiring at least a sub-Hz linewidth clock transition.

The alkaline earth-like atoms (*e.g.* Sr, Ca, Yb) are promising candidates. Consider, for example, the clock transition in atomic strontium ($5s^2\,{}^1S_0 \rightarrow 5s5p\,{}^3P_0$). In ^{87}Sr this transition is weakly allowed with a linewidth of 1 mHz and a saturation intensity of 0.4 pW/cm^2 [32]. The low saturation intensity enables long-baseline configurations (> 10 km) for suitably cold atomic ensembles[3]. In addition to its high Q, this transition is also desirable because it exhibits manageable sensitivity to environmental backgrounds. For example, the blackbody shift has a temperature coefficient of –2.3 Hz(T/300K)[4][33]. At $T = 100$ K, this implies a temperature stability requirement of ; <3 mK/$\sqrt{\text{Hz}}$ for a strain sensitivity of $h = 10^{-20}/\sqrt{\text{Hz}}$ at 10 mHz. For magnetic fields, simultaneous or interleaved interrogation of each of the linear Zeeman sensitive transitions, as described in Ref. [33], results in a residual quadratic Zeeman coefficient of –0.23 Hz/G^2 [33] and also enables measurement of the residual magnetic field. This coefficient is significantly more favorable than that of the Rb interferometers previously analyzed [3]. In principle a second atomic species could be used to independently characterize these shifts in order to provide further suppression. AC Stark shift related backgrounds appear to be negligible. Many other backgrounds are similar to those discussed in Refs. [2] and [3].

3.6 Discussion

This configuration enables a high precision measurement of the relative acceleration between two inertial atom clouds. The high Q atomic transition provides the necessary time reference. The laser is

not used as a clock and thus laser frequency noise does not affect the measurement, unlike all other interferometric gravitational wave detection schemes. Furthermore, an atom is an excellent inertial proof mass. A neutral atom's level structure is universal and is significantly less sensitive to environmental perturbations than conventional macroscopic references such as a laser or a drag-free proof mass, whose physical parameters (thermal and electrodynamic properties) can vary significantly. As we have shown this type of atom interferometer would allow detection of gravitational waves with the same sensitivity as in the proposals described in Refs. [22, 2, 3] but with significantly reduced requirements on laser and platform stability (as in Table 3.1), enabling single-baseline gravitational wave detection.

4. Point Source Interferometry

Light-pulse atom interferometry enables precision tests of gravity [15, 18, 9] and electrodynamics [34] as well as practical applications in inertial navigation, geodesy, and timekeeping. Phase shifts for light-pulse atom interferometers demonstrate sensitivity to the initial velocity distribution of the atom source, often resulting in inhomogeneous dephasing that washes out fringe contrast [35]. In this section, we show that use of spatially resolved imaging in combination with an initially spatially localized atomic source allows direct characterization of these phase shifts. We refer to this technique as point source interferometry (PSI).

The contrast loss associated with such inhomogeneous dephasing is not fundamental, but is a consequence of atom detection protocols that average over velocity-dependent phase shifts. With PSI we establish a correlation between velocity and position and use spatially-resolved detection to form an image of the ensemble that reveals its velocity-dependent phase structure. A simple way to realize this correlation is through ballistic expansion of the ensemble. In the limit that the ensemble size at detection is much larger than its initial size, each atom's position is approximately proportional to its initial velocity. Consequently, any initial velocity-dependent phase shift results in a spatial variation of the interferometer phase, yielding a position-dependent population difference between the two output ports of the interferometer.

An important example of velocity sensitivity is due to rotation of the interferometer laser beams [36, 9]. Rotation at a rate Ω leads to a phase shift (Table 4.1, term 2) that depends on $(\upsilon x, \upsilon y)$, the initial transverse velocity of the atom. In a rotating frame, this effect may be interpreted as a Coriolis acceleration. PSI also allows observation of longitudinal velocity-dependent phase shifts in asymmetric atom interferometers [37] (*e.g.*, Table 4.1, term 3).

To demonstrate PSI, we induce a velocity-dependent phase shift in a ^{87}Rb Raman light-pulse atom interferometer. We launch cold atoms from the bottom of a 10-meter tall vacuum enclosure (Fig. 4.1a) and apply a three-pulse accelerometer sequence ($\pi/2 - \pi - \pi/2$) [21]. The first pulse serves as an atom beamsplitter, coherently driving the atoms into a superposition of states $|F = 1; p\rangle$ and $|F = 2; p + \hbar k_{\text{eff}}\rangle$ with momentum difference $\hbar k_{\text{eff}} = 2\hbar k$. Over the subsequent $T = 1.15$ s interrogation interval, the two parts of the atom's wave function separate vertically by $\hbar k_{\text{eff}}/m\,T = 1.4$ cm (Fig. 4.1b), at which time a mirror pulse reverses the relative momenta and internal states. After an identical drift time, a final beamsplitter pulse interferes the atom wave packets. We then image the atom fluorescence using a pair of CCD cameras located below the interferometry region (Fig. 4.1c). By the time of imaging, 2.6 s after launch, the 50 nK atomic source has expanded to 30 times its original size, establishing the position-velocity correlation necessary for PSI.

We imprint a velocity-dependent phase shift by rotating the atom interferometer laser beam axis at a tunable rate $\delta\Omega$. Figure 4.2 shows typical detected atom distributions for several different values of $\delta\Omega_x$.

The velocity-dependent phase gradient we observe in Fig. 4.2 is proportional to the applied rotation rate (Fig. 4.3). For faster rates, the phase

Term	Phase Shift	Size (rad)
1	$k_{\text{eff}} g T^2$	2.1×10^8
2	$2\mathbf{k}_{\text{eff}} \cdot (\mathbf{\Omega} \times \mathbf{v}) T^2$	5.1
3	$k_{\text{eff}} v_z \delta T$	3.5
4	$\frac{\hbar k_{\text{eff}}^2}{2m} T_{zz} T^3$	0.44
5	$k_{\text{eff}} T_{zi} (x_i + v_i T) T^2$	0.18
6	$\frac{1}{2} k_{\text{eff}} \alpha (v_x^2 + v_y^2) T^2$	0.04

Table 4-1: Velocity dependent phase shifts and their sizes assuming the following: $k_{\text{eff}} = 2k = 2 \cdot 2\pi/780$ nm, $T = 1.15$ s, initial velocity spread $\upsilon_i = 2$ mm/s (50 nK), initial positions $\chi_i = 200$ µm, $|\Omega| = 60$ µrad/s, gravity gradient tensor components $T_{zi} = 3075$ E, interferometer pulse timing asymmetry $\delta T = 100$ µs, and wavefront curvature $\alpha = (\lambda/10)/\text{cm}^2$. Note that for $T_{zx}, T_{zy} = 50$ E the size of term 5 is significantly smaller. The acceleration (term 1) and gravity curvature (term 4) phase shifts are shown for reference.

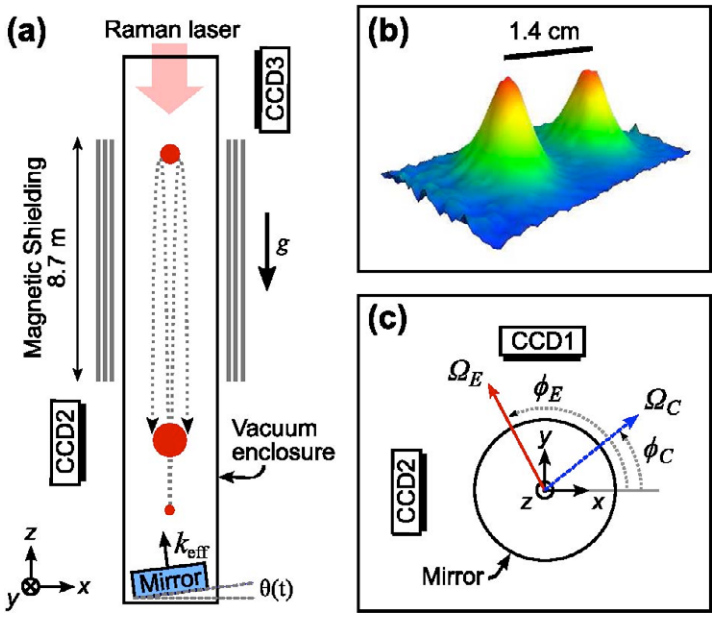

Figure 4-1: (a) Schematic diagram of the apparatus, viewed from the side. The atom cloud (red circle) is cooled and launched from below the magnetically-shielded interferometry region. The two interferometer output ports are imaged by both perpendicular cameras (CCD1 and CCD2). All interferometry pulses are delivered from the top of the tower and are retroreflected off a mirror (at angle θ(t)) resting on a piezo-actuated tip-tilt stage. (b) Image of the ensemble after a beamsplitter pulse showing the separation between two halves of the atomic wavepacket. For this shot we launched the atoms with extra velocity to reach CCD3. (c) Top view of the tip-tilt stage and lower cameras with the direction and magnitude of the Earth rotation Ω_E and an (arbitrary) applied counter-rotation Ω_C.

shift is large enough that multiple fringe periods appear across the ensemble. Without spatially resolved detection, averaging over these fringes would yield negligible contrast. With PSI, we realize record duration atom interferometry, even in the presence of large rotation rates

To create the cold atomic source, we load 4×10^9 atoms from a magneto-optical trap into a plugged quadrupole trap, where we evaporate with a microwave knife [39, 40]. A magnetic lensing sequence in a time-orbiting potential (TOP) trap collimates the atom source in 3D, cooling and expanding the cloud while maintaining high phase space density[1] . The final cloud contains 4×10^6 atoms at 50 nK with an initial radius of 200 µm. Alternatively, we can produce clouds at 3 nK with 10^5 atoms and an initial radius of 30 µm by evaporating in a TOP trap with a microwave knife prior to the magnetic lensing sequence.

A microwave pulse transfers the ultracold atoms into a magnetically-insensitive Zee-man sublevel. They are then coherently launched with an optical lattice [43], which transfers 2386 photon momenta with a peak acceleration of 75 g. They enter the in¬terferometer region, a 10 cm diameter, 8.7 m long aluminum vacuum tube. A solenoid wound around the tube provides a bias magnetic field, and three layers of magnetic shielding suppress the environmental field to < 1 mG [44].

A small fraction of the atoms are launched into ±2lk momentum states. We purify the ensemble's vertical momentum with a 135 µs Raman π-pulse, which transfers a 25 nK

(0.1 *hk*) subset of the ensemble into $|F=1\rangle$. A short pulse resonant with $|F=2\rangle \rightarrow |F'=3\rangle$ blows away atoms that did not transfer.

A pair of fiber-coupled 1 W tapered amplifiers (TAs) generate the retroreflected interferometer pulses. The seeds for the two TAs are derived from a common source cavity-stabilized to a linewidth of < 1 kHz and detuned 1.0 GHz blue from the 780 nm D_2 line ($|F=2\rangle \rightarrow |F'=3\rangle$). The seed for one TA passes through a fiber phase modulator that generates the 6.8 GHz sideband necessary for Raman interferometry. An acousto-optic modulator (AOM) chirps the other seed to correct for the atoms' Doppler shift. The output of the TAs are combined on a polarizing beamsplitter cube, and the copropagating beams are diffracted by an AOM that acts as a fast optical switch. The beamsplitter and mirror pulses are 35 µs and 70 µs in duration, respectively. The beams have a 2cm $1/e^2$ intensity radial waist. The relative power of the two beams is chosen empirically to suppress intensity-dependent detunings by balancing AC Stark shifts (to < 2 kHz).

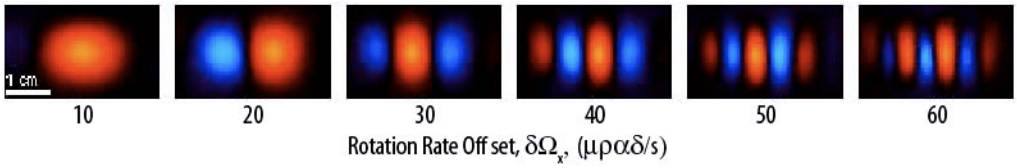

Figure 4-2: Spatial fringes on the atom population observed on CCD2 versus rotation rate offset $\delta\Omega_x$. Blue versus red regions show anti-correlation in atom population. The second output port, with fringes π rad out of phase, is not shown. Each image is the second-highest variance principle component arising from a set of 20 measurements [38].

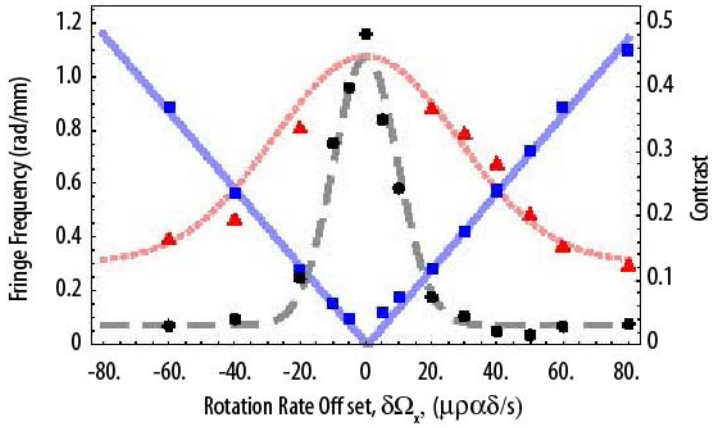

Figure 4-3: Fringe spatial frequency (blue squares, solid line) and contrast versus applied rotation for the data in Fig. 4.2. The fitted slope of the fringe spatial frequency is consistent with term 2 of Table 4.1 to < 10%. Fringe contrast is observed over a wide range of rotation rates (red triangles, dotted line Gaussian fit), while the contrast from integration detection decays rapidly (black circles, dashed line Gaussian fit)..

Prior to detection, we spatially separate the output ports by applying a short pulse (~ 50 photon recoils) resonant with $|F=2\rangle \rightarrow |F'=3\rangle$. We wait 50 ms before simultaneously halting and imaging the atoms with a 2 MHz red-detuned beam. The atoms are nearly at rest after the first 300 μs of the 5 ms imaging time. The scattered light is collected by two orthogonal CCD cameras, each with a numerical aperture of 0.25 (Fig. 4.1c). The time from initial atom loading to the final image is 20 s.

We precisely control the direction of the interferometer beams with an in-vacuum, piezo-actuated tip-tilt stage onto which the retroreflection mirror is kinematically constrained. The stage has 1 nrad measured precision and a range of 400 μrad. The stage platform is secured kinematically to three nanopositioners (Nano-OP30; Mad City Labs) by stiff springs. The nanopositioners are bolted to the vacuum enclosure, which is anchored to the vibrationally-quiet (10^{-8} g/$\sqrt{\text{Hz}}$) concrete floor.

The rotation of the Earth is a significant source of velocity-dependent phase shifts. At our latitude in Stanford, California, the effective rate is Ω_E = 57.9 μrad/s, which induces fringes of periodicity similar to the highest rotation rate in Fig. 4.2. With the tip-tilt stage we apply a compensating rotation of equal and opposite magnitude ($\Omega C = -\Omega_E$) to eliminate these phase shifts [35, 9, 45]. We implement this rotation by incrementing the mirror's angle in discrete steps between each interferometer pulse. In Figs. 4.2 and 4.3 we add a variable rotation rate $\delta\Omega x$ to this nominal rotation compensation vector.

Figures 4.4a and 4.4b show images of both output ports for a rotation-compensated interferometer using two atom source temperatures. The interferometer in Fig. 4.4a (3 nK) has an integrated interferometer contrast of 80% while that in Fig. 4.4b (50 nK) shows a contrast of 48% [2] . The contrast is reduced for the hotter source because of Rabi pulse area inhomogeneities due to larger horizontal cloud diameter (with respect to the spatially nonuniform laser beam intensity) and larger Doppler width.

With PSI, we maintain spatial fringe contrast even in the presence of large net rotation rates (Fig. 4.3). By comparison, the conventional integrated contrast for the same data decays rapidly with increasing rotation rate because a spatial average over the fringe pattern washes out the interference. The reduction in the PSI fringe contrast at higher rotation rates is not fundamental, but results from heating during imaging and imperfect alignment between the applied rotation $\delta\Omega$ and the camera line-of-sight.

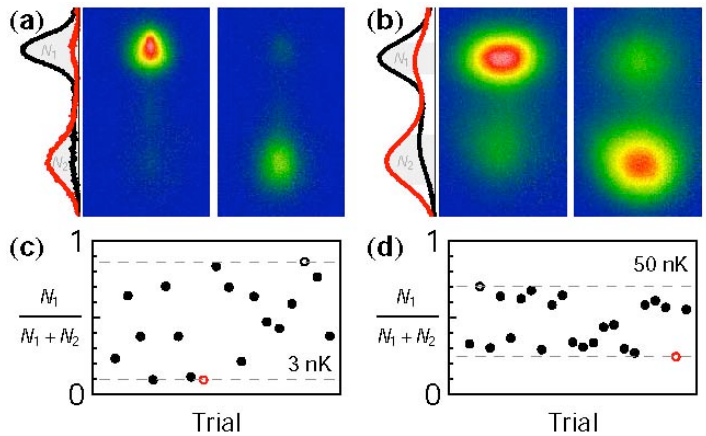

Figure 4-4: Images of the interferometer output ports using (a) 3 nK and (b) 50 nK atom sources with rotation compensation ($\Omega_C = -\Omega_E$). The upper (lower) port consists of N1 (N2) atoms in state $|F=1\rangle$ ($|F=2\rangle$). Each pair of images represents the two extremes in the observed population ratio, $N_1/(N_1+N_2)$ (open circles in (c) and (d)). Population ratio variations between trials re¬flect interferometer phase variations caused by vibration of the retroreflec¬tion mirror. Also shown in (a) and (b) are the atom densities integrated horizontally for the two images (black and red curves), with the shaded regions used to determine the port atom numbers, N_i. The lower port has been optically pushed, resulting in a hotter cloud with fewer peak counts. Both ports are heated by a 5 ms imaging pulse. This heating is most evident for 3 nK clouds.

To compute spatial fringe contrast in Fig. 4.3, we divide the fitted amplitude of the population fringes by the fitted amplitude of the underlying cloud [38]. While fringes are visible on each raw image, we use Principal Component Analysis (PCA) as a filter to isolate the population fringe from the cloud shape in a model-independent way for more robust fits [46]. The fitted fringe frequency provides the magnitude of the phase gradient.

We also measure the rotation rate of the Earth. After coarsely compensating for the Earth's rotation with the tip-tilt stage, we tune the applied rate by adding a small rotation $\delta\Omega_E \equiv \Omega_C - \Omega_E$ along the nominal direction of true North ($\phi_C \approx \phi_E + \pi$). We observe the resulting phase gradient simultaneously on CCD1 and CCD2. The magnitude of the observed phase gradient depends on the projection of the net rotation rate onto each camera (see Fig. 4.1c). To detect small phase gradients that generate less than 2π radians of phase across the ensemble, we extract the differential phase $\Delta\Phi$LR by splitting each image about a vertical line and analyzing the left and right halves as independent interferometers.

Figure 4.5a shows $\Delta\Phi$LR as a function of $\delta\Omega_E$ as observed on CCD1 and CCD2. Each measurement is the result of 20 interferometer cycles. We parametrically plot the population ratio of the left half versus the right (*e.g.*, Fig. 4.5b) and extract the differential phase and contrast using an ellipse fitting procedure [30]. Occasional trials (< 5%) that display no interference appear at the center of the ellipses and are rejected. The horizontal intercept of a linear fit to this data provides a measurement of Earth's rotation rate with a precision of 200 nrad/s.

The difference in the intercepts observed by the two cameras indicates that the ro¬tation compensation direction ϕ_C is slightly misaligned from true North ϕ_E such that $\Delta\phi \equiv \phi_C - (\phi_E + \pi) \neq 0$. This results in a spurious rotation $(\Delta\phi\ \Omega_E \sin\phi_E)\hat{x}$ imprints a phase gradient visible on CCD2 (see Table 4.1, term 2) independent of $\delta\Omega_E$. Likewise, a spurious rotation $(-\Delta\phi\ \Omega_E \cos\phi_E)\hat{Y}$ imprints a phase gradient visible on CCD1. The slopes for the two cameras in Fig. 4.5 are different because of unequal projection of Ω_E and small differences in the projected widths of the ensemble.

Although the mean interferometer phase is dominated by seismic noise contributions at long T, we can infer an acceleration sensitivity using the observed differential phase noise between different parts of the imaged cloud. We divide the output port images using a checkerboard grid and study the differential phase between the combined even and combined odd grid squares. Varying the grid size s in this analysis reveals correlated phase noise at different spatial scales [3] . Analyzing 280 trials with $\Omega_C \approx -\Omega_E$, we find the differential even-odd phase noise is 2.0 mrad per shot for grid sizes below s = 3 mm.

Combined with the acceleration response (Table 4.1, term 1), this implies an acceleration sensitivity of 6.7×10^{-12}g in one shot[4], an improvement of more than two orders of magnitude over previous limits [47]. By comparison, the atom shot-noise limit for the 4×10^6 atoms used in this interferometer at 50% contrast is $\sim 4 \times 10^{-12}$g in one shot. Note that this grid analysis rejects low spatial frequency varia-

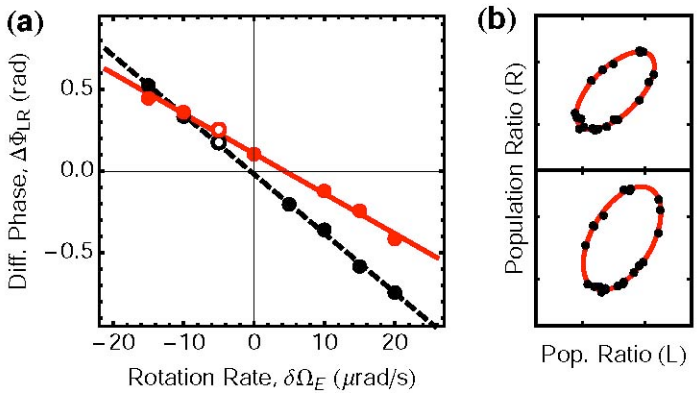

Figure 4-5: (a) PSI dual-axis gyroscope. We extract the differential phase ΔΦLR between the left and right sides of the ensemble as a function of the rotation rate δΩE, as measured on cameras CCD1 (black, dashed) and CCD2 (red, solid). (b) Sample ellipses emerging from the right-versus-left population ratios of CCD2 (upper) and CCD1 (lower), corresponding to the open circles of part (a).

tions of the phase across the cloud that originate, for example, from fluctuations in initial kinematics. The results are applicable to measurements where these effects are expected to be common, such as for overlapped ensembles of two species of atoms in an equivalence principle test.

PSI does not require a 10-meter apparatus. A dual-axis gyroscope with shot-noise limited rotation noise of 100 μdeg $/\sqrt{\text{hour}}$ hour can be realized with 10^6 atoms prepared at 3 mK in an interferometer with T = 10ms and $4\hbar k$ atom optics cycling at 25 Hz (with atom recapture).

PSI can measure the interferometer beam optical wavefront in situ. This is desirable in precision atom interferometry applications, including gravitational wave detection [3]. Each atom in an expanding ensemble samples the laser phase at three locations, thereby measuring wavefront aberrations. Term 6 of Table 4.1 models the interferometer response to a parabolic wavefront curvature of the form $k\alpha(\chi^2 + y^2)/2$. Our measured phase noise implies a wavefront sensitivity of $\alpha \sim \lambda/500/\text{cm}^2$ in one shot.

Finally, PSI allows measurement of multiple components of the gravitational gradient tensor (Table 4.1, term 5). The sensitivity we report is also sufficient to observe the gravity curvature induced phase shift (Table 4.1, term 4) [48]. Such sensitivity enables precision tests of the equivalence principle and general relativity [9, 18].

5. Enhanced Atom Interferometer Readout through the Application of Phase Shear

Light-pulse atom interferometers use short optical pulses to split, redirect, and interfere freely-falling atoms [49]. They have proven widely useful for precision metrology. Atom interferometers have been employed in measurements of the gravitational [15, 31] and fine-structure [34] constants, in on-going laboratory tests of the equivalence principal [9] and general relativity [10, 50], and have been proposed for use in gravitational wave detection [2, 1]. They have also enabled the realization of high performance gyroscopes [35], accelerometers [6], gravimeters [36], and gravity gradiometers [14].

Current-generation light-pulse atom interferometers determine phase shifts by recording atomic transition probabilities [49]. These are inferred from the populations of the two atomic states that comprise the interferometer output ports. Due to experimental imperfections, interference contrast is not perfect – even at the extremes, the dark port does not have perfect extinction. This results in the need to independently characterize contrast prior to inferring phase. Typically, this is done with a sequence of multiple shots with different phases, such that the population ratio is scanned through the contrast envelope [51]. Such an experimental protocol relies on the stability of the contrast envelope. In many cases, the contrast varies from shot to shot, introducing additional noise and bias in the phase extraction process.

We present a broadly applicable technique that is capable of resolving interference phase on a single experimental shot. This is accomplished through the introduction of a phase shear across the spatial extent of the detected atom ensemble. The shear is manifest in a spatial variation of the atomic transition probability, which, under appropriate conditions, can be directly observed in an image of the cloud [Fig. 4.1(b)]. Using this phase shear readout (PSR), it is no longer necessary to vary the phase

over many shots to determine the contrast envelope. Instead, the contrast of each shot can be inferred from the depth of modulation of the spatial fringe pattern on the atom ensemble. The interferometer phase is directly determined from the phase of the spatial fringe.

The analysis of PSR fringes reveals rich details about atom interferometer phase shifts and systematic effects, much as the analysis of a spatially varying optical interference pattern yields information about the optical system and its aberrations. The intentional application of a phase shear is analogous to the use of an optical shear plate, where a large applied phase shear highlights small phase variations across a laser beam.

In this work, we show that beam pointing can be used to introduce shear in a way that is broadly applicable to existing interferometer configurations. In particular, this method does not require Bose-Einstein condensed or ultra-cold atomic sources. We demonstrate the power of PSR by implementing a precise atom interferometer gyrocompass. We also show how laser beam pointing and atom-optics pulse timing asymmetry can be combined to provide arbitrary control over the phase shear axis in the limit where the atoms expand from an effective point source.

The apparatus and methods are similar to those of our previous work [52]. Using evaporative cooling followed by a magnetic lens, we obtain a cloud of 4×10^6 ^{87}Rb atoms with a radius of 200 µm and a temperature of 50 nK. These atoms are prepared in the magnetically insensitive $|F=2, m_F=0)$ state, and then launched vertically into an 8.7 m vacuum tube with a chirped optical lattice. The atoms fall back to the bottom after 2.6 s, and we then use a vertical

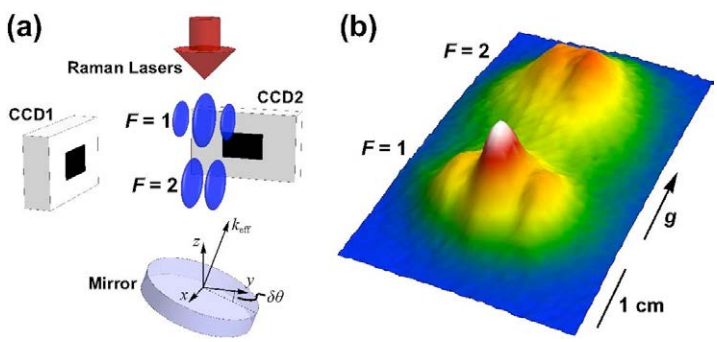

Figure 5-1: (a) Schematic diagram of the apparatus, showing beam-tilt phase shear readout. Atoms are cooled and launched upward into an interferometer region, not shown. Once they fall back to the bottom, the wavepackets are overlapped and an interference pattern (blue fringes) is imaged by two perpendicular cameras (CCD1,2). An additional optical pulse is used to separate the two output ports ($F = 1$ and $F = 2$) by pushing the $F = 2$ atoms downwards. All atom optics pulses are performed by lasers incident from above and retroreflected off of a piezo-actuated mirror. Tilting this mirror by an angle δθ for the third atom optics pulse yields a phase shear. (b) A fluorescence image of the atomic density distribution taken with CCD2 after interference. Spatial fringes result from a third-pulse tilt $\delta\theta = 60$ µrad about the x-axis. The pushed $F = 2$ atoms are heated, yielding reduced apparent contrast, and we ignore the $F = 2$ output port in subsequent analysis.

fluorescence beam to image them onto two perpendicular CCD cameras (Fig. 5.1).

While the atoms are in free-fall in a magnetically shielded region [44], we perform light-pulse atom interferometry with a $\pi/2$ $-\pi$ $-\pi/2$ acceleration-sensitive configuration with an interferometer duration of $2T = 2.3$ s. The atom optics pulses are applied along the vertical axis using two-photon Raman transitions between the $|F=2, m_F=0)$ and $|F=1, m_F=0)$ hyperfine ground states (the lasers are detuned 1.0 GHz blue of the $|F=2) \rightarrow |F'=3)$ transition of the D_2 line). The atom optics light is delivered from above and retroreflected off of an in-vacuum piezo-actuated tip-tilt mirror.

The effective wavevector k_{eff} of the Raman transitions is determined by the pointing direction of the retroreflection mirror [9], which is set by the piezo stage for each atom-optics pulse with 1 nrad precision. We compensate for phase shifts arising from the rotation of the Earth by applying additional tilts to each of the three pulses, as described in Refs. [9, 52], but the mirror angle can also be used to induce shear for PSR.

To generate a controlled phase shear, we tilt the mirror for the final $\pi/2$ pulse by an angle δθ with respect to the initial two pulses (in addition to the tilts needed for rotation compensation). In the semi-classical limit, the phase shift for a three-pulse interferometer is $\Delta\Phi = k_1 \cdot x_1 - 2k_2 \cdot x_2 + k_3 \cdot x_3$, where $k_i \equiv k_{eff,i}$ is the effective propagation vector at the time of the ith pulse and xi is the classical position of the atom [51, 49]. For example, tilting k_3 by an additional angle δθ about the *x*-axis yields a phase $\Phi_H = k_{eff}\, \delta\theta\, y_3$ across the cloud, where y_3 is the horizontal position at the third pulse [Fig. 5.1(a)]. This

phase shear is independent of the details of the previous atom-laser interactions and of the implementation of the atomic source (in particular, its spatial extent, temperature, and quantum degeneracy).

Figure 5.1(b) shows an image of the interferometer output that results from this horizontal phase shear, with $\delta\theta$ = 60 µrad. An optical "pushing" pulse, 5 µs long and resonant with the $|F=2\rangle \rightarrow |F'=3\rangle$ transition, separates the interferometer output ports. Complementary fringes appear across each port, corresponding to the spatial variation of the atomic transition probability that results from phase shear. For linear shears, the atom distribution at each port is modulated by an interference term $P(\mathbf{r}) = {}^1/_2 + {}^C/_2 \sin(\kappa \cdot \mathbf{r} + \phi 0)$, where C is the contrast, $\phi 0$ is the overall interferometer phase, and κ is the wavevector of the spatially varying component of the phase.

Since the retroreflection mirror can be tilted about an arbitrary horizontal axis, beam-tilt PSR can yield fringe patterns with $\hat{\kappa}$ anywhere in the *xy* plane, orthogonal to the laser beam axis [see Fig. 5.1(a)]. For instance, it is possible to choose a tilt axis parallel to the line-of-sight of either of the CCD cameras (which are perpendicular), in which case we see a spatial fringe pattern with one camera, but no contrast with the other. Hereafter, we tilt about the *x*-axis, yielding fringes on CCD2.

The spatial frequency κ of beam-tilt PSR fringes is set by the tilt angle $\delta\theta$. Figure 5.2(b) shows the expected linear dependence, and it is apparent that by appropriate choice of the shear angle, the period of the shear can be tuned to an arbitrary value. While high spatial frequencies are desirable, in practice spatial frequency is limited by the depth of focus of the imaging system. Because we detect the atoms at a final drift time t_d =2.7 s that is later than the third pulse time t_3 =2.5 s (both measured from the time of trap release), we must correct for the continued motion of the atoms. In the limit where the initial size of the atomic source is much less than the final spatial extent of the atomic cloud (point source limit [52, 53]), the position at t_d of an atom with velocity υy is $y \approx \upsilon y t_d \approx y_3\, t_d/t_3$. The detected

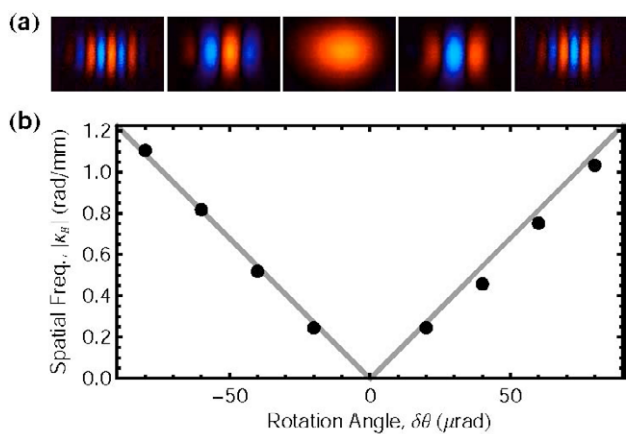

Figure 5-2: Horizontal fringes resulting from beam-tilt PSR in a 2 T =2.3 s interfer¬ometer. (a) Spatial fringes observed on CCD2 with third-pulse tilt angles $\delta\theta = -80, -40, 0, +40, +80$ µrad (from left to right). Red versus blue regions show anti-correlation in atom population. Each image is the second-highest variance principal component arising from a set of 20 fluorescence images [52]. (b) Measured fringe spatial frequency $|\kappa_H|$, resulting from images filtered using principal component analysis [52]. We bin the images vertically and fit a Gaussian modulated by the interference term $P(\mathbf{r})$. The curve is a theoretical prediction with no free parameters.

horizontal fringe spatial frequency is then $\kappa_H \equiv \partial_y \Phi_H = k_{eff}\, \delta\theta\, t_3/t_d$.

To demonstrate single-shot phase readout, we implement a short interferometer sequence (2 T = 50 ms) near the end of the drift time. In this case, the atom cloud has a large spatial extent for the entire pulse sequence. For each shot, we set the interferometer phase with an acousto-optic modulator and read it back using beam-tilt PSR with $\delta\theta$ = 60 µrad. Figure 5.3 shows the expected correspondence between the applied and measured phases. The spread in the measured phase is due to technical noise associated with spurious vibrations of the optics for the laser beams that drive the stimulated Raman transitions.

As an example of how PSR can enable a precision measurement, we implement an atom interferometric gyrocompass in a long interrogation time (2T =2.3 s) configuration. In this case, the Raman laser axis is rotated to compensate Earth's rotation, keeping this axis inertially fixed throughout the interrogation sequence. At the latitude of our lab in Stanford, California, this corresponds to an effective rotation rate of Ω_E = 57.9 µrad/s about an axis along the local true North vector, which we take to be at angle ϕE with respect to the *x*-axis. However, a small misalignment $\delta\phi_E \ll 1$ between the rotation axis of the retroreflection mirror and true North results in a residual rotation $\delta\Omega \approx \delta\phi_E\, \Omega_E\, (\sin\phi_E - \cos\phi_E \hat{y})$ that leads to a Coriolis phase shift $\phi_C = 2\mathbf{k}_{eff} \cdot (\phi\Omega \times \mathbf{v})\, T^2$ that varies across the cloud. As before, in the point source limit $vy \approx y/t_d$, so the Coriolis phase gradient is $\kappa_C, y \equiv \partial_y \Phi_C = 2k_{eff} T^2 \delta\phi E \Omega_E \sin\phi_E/t_d$. To realize a gyrocompass, we vary the axis of applied rotation by scanning $\delta\phi_E$, and identify true North

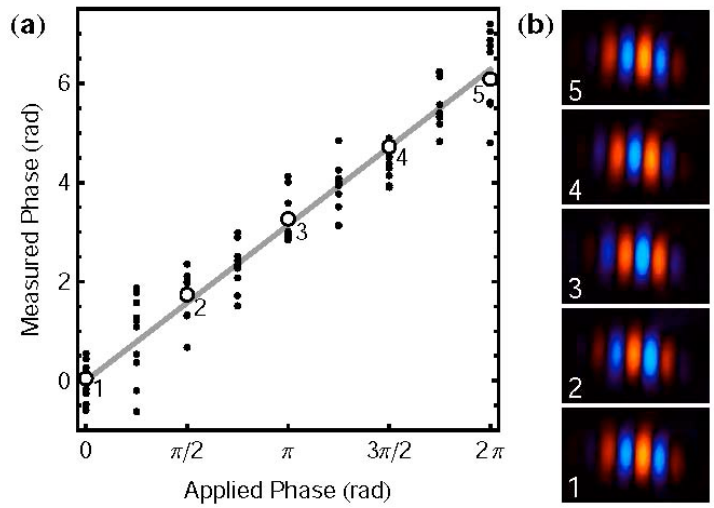

Figure 5-3: Demonstration of single-shot phase readout with a 2 T = 50 ms interferometer. (a) Measured phase versus the applied phase of the final atom-optics pulse for 96 shots. A line with unity slope is shown for reference. The measured phase is fit from images like those in (b). The measurement scatter at each phase step is dominated by technical noise introduced by vibration of the Raman laser beam delivery optics. (b) Five sample interferometer shots [open circles in (a)], separated in measured phase by ~ π/2 rad. All images are filtered with principal component analysis.

with the angle at which $\kappa_{C,y} = 0$.

It can be challenging to measure small phase gradients with spatial frequencies $\kappa \ll 1/\sigma$, where σ is the width of the atom ensemble. In this limit, there is much less than one fringe period across the cloud, so the fringe fitting method shown in Fig. 5.2(b) cannot be used. Instead, the gradient can be estimated by measuring phase differences across the ensemble (e.*g.*, with ellipse fits [30]), but this procedure can be sensitive to fluctuations in the atomic density distribution (width, position, and shape).

To circumvent these issues, we take advantage of PSR by applying an additional phase shear that augments the residual Coriolis shear Φ_C . An additional tilt of $\delta\theta = \pm 60$ µrad about the x-axis is added before the final interferometer pulse. This introduces a horizontal shear Φ_H with approximately 2.5 fringe periods across the cloud, visible on CCD2. Depending on the sign of the tilt angle, this shear adds to or subtracts from C . The combined phase gradient is then $\kappa\pm \equiv k_{eff}\,|\delta\theta|\, t_3/t_d \pm \kappa_{C,y}$ and is large enough to use fringe fitting to extract the spatial frequency. This technique of shifting a small phase gradient to a larger spatial frequency is analogous to a heterodyne measurement in the time domain. In both cases, the heterodyne process circumvents low frequency noise. By alternating the sign of the additional 60 µrad tilt, a differential measurement is possible whereby systematic uncertainty in the applied shear angle is mitigated: $\Delta\kappa \equiv \kappa_+ - \kappa_- = 2\kappa_{C,y}$, independent of the magnitude of $\delta\theta$.

Figure 5.4 shows the expected linear scaling of the differential spatial frequency $\Delta\kappa$ as a function of the applied rotation angle $\delta\phi_E$. A linear fit to the data yields a horizontal intercept that indicates the direction of true North with a precision of 10 millidegrees. We note that an apparatus optimized for gyrocompass performance could achieve similar or better precision in a more compact form factor. Also, this method does not require a vibrationally stable environment since the measurement rests on the determination of the fringe period, not the overall phase.

Finally, we show how combining beam tilts and interferometer timing asymmetries provides nearly arbitrary control over the spatial wavevector κ of the applied shear. While a beam tilt applies a phase shear with spatial wavevector in the plane transverse to the interferometer beam axis, interferometer timing asymmetry yields a phase shear parallel to the beam axis ($\kappa \mathrm{I}\, \mathbf{k}_{eff}$) in the point source limit [37]. To create an asymmetric interferometer, we offset the central π pulse by $\delta T/2$ such that the time between the first and second pulses ($T + \delta T/2$) is different from the time between the second and third pulses ($T - \delta T/2$). The resulting phase shift, $\Phi_V = k_{eff}\, \upsilon_z \delta T$, depends on the atoms' Doppler shift along the direction of k_{eff}. The phase shear at detection is then $\kappa_V = \partial_z \Phi_V = k_{eff}\, \delta T/t_d$. Figure 5.5(a) shows the resulting vertical fringes, which are orthogonal to those from beam tilts seen in Fig. 5.2(a) and are simultaneously visible on both CCD cameras. The fitted fringe frequency shown in Fig. 5.5(c) exhibits the expected linear dependence as a function of δT , deviating at low spatial frequency due to the

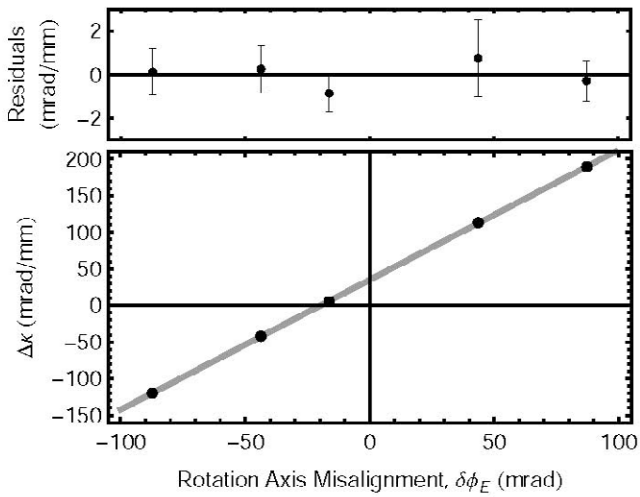

Figure 5-4: Gyrocompass using the phase shear method. Each Δκ point is the coronation of 40 trials, 20 at each of the two applied tilt values ($\delta\theta = \pm 60$ μrad). The horizontal intercept of a linear fit gives the direction of true North. .

difficulty of fitting a fringe with $\kappa \sim 1/\sigma$.

For these vertical fringes, we find that the imaging pulse reduces the detected spatial frequency by stretching the cloud vertically. We independently characterize this stretch by measuring the vertical fringe period as a function of imaging duration τ and then extrapolating to $\tau = 0$. The results indicate a fraction stretch rate of $\alpha = 0.12\ \mathrm{ms}^{-1}$. The modified prediction for the spatial frequency is $\kappa 8V = \kappa V / (1 + \alpha\tau)$. With the $\tau = 2$ ms imaging time used, this agrees well with the measurements of Fig. 5.5(c) with no free parameters.

By combining beam tilt shear κ_H with timing asymmetry shear κ_V, we can create spatial fringes at arbitrary angles. The composite phase shear is at an angle $\Theta = \arctan(\kappa_V / \kappa_H) = \arctan[\delta T / (\delta\theta\ t_3)]$. Figures 5.5(b) and (d) show the fringe images and extracted angles using a $\delta\theta = 40$ μrad beam tilt combined with a range of timing asymmetries. To find the angles, we apply Fourier and principal component filters and fit with a two-dimensional Gaussian envelope modulated by an interference term P (**r**). Because the vertical stretch imparted by the imaging beams modifies the measured angle, we again correct for image stretching during detection. The modified prediction, $\Theta = \mathrm{arccot}[(1 + \alpha\tau)\cot\Theta]$,

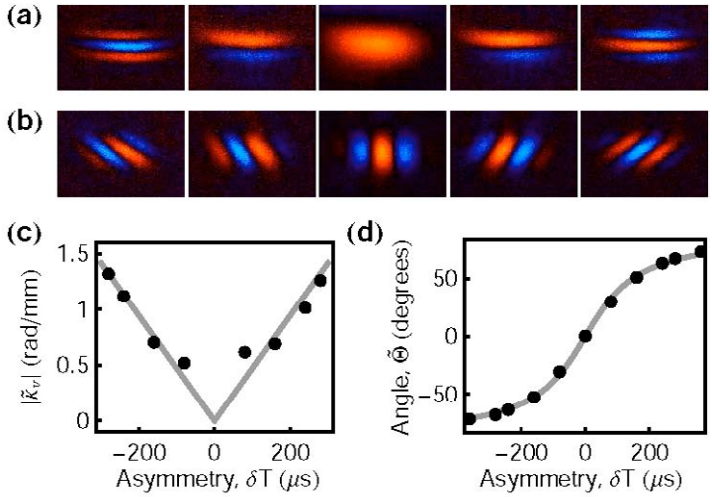

Figure 5-5: Arbitrary control of spatial fringe direction. (a) Second-highest variance principal components from sets of 20 trials with timing asymmetry $\delta T = -240, -160, 0, +160, +240$ μs (from left to right) (b) Comparable images for trials with both a beam tilt $\delta\theta = 40$ μrad and $\delta T = -160, -80, 0, +80, +160$ μs. (c) Measured fringe spatial frequency extracted from fits to principal component filtered images with vertical fringes. (d) Measured fringe angle extracted from fits to images with tilted fringes. In both (c) and (d) the curves are predictions with no free parameters.

shows good agreement with the measured angles of Fig. 5.5(d) with no free parameters.

We have demonstrated a precision gyrocompass with PSR, but with arbitrary control of the shear angle the method can be used to measure phase shifts and gradients from any origin. For example, a vertical gravity gradient T_{zz} induces a phase shear $k_{\mathrm{eff}}\, T_{zz} \upsilon_z T^3$. This shear translates the measured angles of Fig. 5.5(d) such that $\Theta = \arctan\, [(\delta T - T_{zz} T^3)/\, (\delta\theta\ t_3)$. For our parameters, this would yield an effective asymmetry of 2 ns/E. PSR can also be used to measure nonlinear phase variations, including optical wavefront aberrations [52]. Finally, we expect the phase shear method to be enabling for future inertial sensors operating on dynamic platforms, where single shot estimation of phase and contrast is vital.

Appendix A.

Atom Interferometry Primer

A general introduction to atom interferometry is provided here as background. For a detailed discussion of how to calculate phase shifts in atom interferometry, see [9]. For a treatment of atom interferometry relevant to the detection of gravitational waves specifically, see [2].

A.1. Optical Interferometry

"What is an optical interferometer and what is its use?"

As shown in Figure A.1, the basic principle of an optical interferometer is that a coherent electromagnetic wave (laser) is split into two paths, redirected, and recombined and the relative phase or Optical Path Difference (OPD) between the two paths is measured. A beam splitter is used to split the laser beam, and the two beams are redirected using mirrors. Recombining the beams is done using beam splitters.

Figure A.1 shows a generic optical interferometer. There are two out ports for this interferometer. The interferences at port one and two are:

$$I_{Port_1} = I_1 + I_2 + 2\sqrt{I_1 I_2} Cos(\frac{2\pi}{\lambda} OPD + \varphi) \quad \text{(E.1)}$$

$$I_{Port_2} = I_1 + I_2 - 2\sqrt{I_1 I_2} Cos(\frac{2\pi}{\lambda} OPD + \varphi) \quad \text{(E.2)}$$

I_{Port_1} and I_{Port_2} are total intensities at port one and two. I_1 and I_2 are intensities in the two paths after beam splitting. OPD is the Optical Path Difference between the two paths. λ is the wavelength of the laser. φ is the controlled phase, which can be changed in time to values 0, 90, 180, and 270 degree for phase shifting. This process is not necessary to measure OPD but greatly improves measurement precision. To get good contrast for interferometry, I_1 and I_2 are equal in intensity, so the equation above can be written as:

$$I_{Port_1} = 2I_0(1 + Cos(\frac{2\pi}{\lambda} OPD + \varphi)) \quad \text{(E.3)}$$

$$I_{Port_2} = 2I_0(1 - Cos(\frac{2\pi}{\lambda} OPD + \varphi)) \quad \text{(E.4)}$$

Generally, one path of the interferometer is the reference path with known optical surfaces and the second path is the test optical component. Control of is done through motion of the reference mirror. Note that Figure A.1 is a Space-Space diagram.

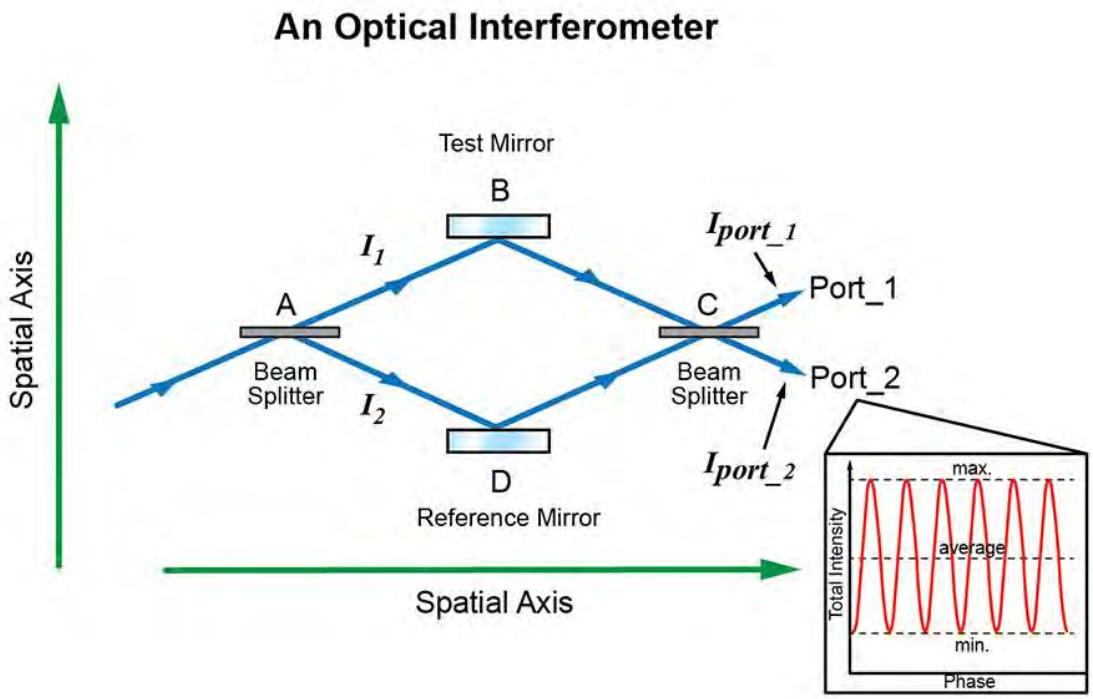

Figure A.1. An Optical Interferometer

Optical interferometers are used to measure surfaces, displacements, and absolute lengths. In this case, the desired information is the surface or position of object(s). The desired information about the object is encoded in the reflected light and the interference of the two coherent light beams results in a change of intensity as a function of the controlled phase φ. This intensity variation is referred to as an interference fringe pattern or "fringes." Fringes are analyzed and are measured.

In optical interferometry, noise is mostly from the environment; vibration and acoustic sources are problematic. $\emptyset PD$ can be enhanced using multiple reflections from the test surface. However, due to practicality and/or for some interferometer configurations, multiple reflections are generally limited to four. Current optical interferometers used in measuring large telescope mirrors have repeatability of 4 nm root mean square (RMS) for an average of 50 measurements, or an RMS of 28 nm per measurement. To minimize issues from vibration, measurements are spatially phase shifted rather than temporally. The fringes at port one and port two are complimentary to each other. Because energy through the interferometer is conserved, if the intensity at port one is zero, intensity is at its maximum at port two for the same controlled phase .

A.2. Atom Interferometry

"Why move away from optical interferometry and into using atom interferometry?"

Over the past decade there has been tremendous progress toward using neutral atoms in measurement devices. Atoms can have a better reproducibility, repeatability, and accuracy than any manmade instrument. Atoms in their own inertial frame are almost completely decoupled from their environment, so their noise floor can be lower than optical interferometers. In this frame (free fall), neutral atoms are excellent test particles for measuring gravitational fields. They can be used to measure the gravity gradient field of the Earth, Moon, other planets, or a gravitational wave emanating from a merger of two black holes.

Atoms have both internal and external degrees of freedom. The internal degrees are different atomic energy levels and the external ones are the different momentum states the atoms can occupy. These multiple degrees of freedom offer flexibility and support a diverse variety of techniques that can be used to amplify the desired signal of an atom interferometer. This is somewhat analogous to the amplification that can be achieved in an optical interferometer by increasing the by using multiple reflections. Recent work demonstrated an atomic interferometer with a more than 50-fold amplification of the desired signal [8].

A.3. What is an atom interferometer?

An atom can operate as an interferometer. To form an interferometer, two coherent waves are required. In an optical interferometer, the two coherent waves are generated by a beam splitter that splits the original electromagnetic wave (laser) into two paths. A material optical component, such as a beam splitter, splits a wave to two portions. In an atom interferometer, the two coherent waves are the two coherent states of the atom. The two states of the atom become coherent by applying a laser pulse to the initial state of the atom. This pulse is analogous to a beam splitter in optical interferometry. In atom interferometry, the coherent waves are material waves called *de Broglie waves*, and the beam splitter is a laser pulse electromagnetic wave.

In atom interferometry, the material optical components such as beam splitters, combiners, and mirrors, are replaced by laser pulses. For example, the electromagnetic wave (laser) is replaced by de Broglie waves (material waves). Generating coherence between the two independent states of the atom is called the *superposition state* of the atom. Atom interferometry is manipulation of the superposition state and its interference with itself via laser pulses.

Information in optical interferometer is on the test mirror and is encoded to the laser light via its reflection from it. The interference of the laser light with itself reveals the encoded . Information in atom interferometer is on the laser pulses and is encoded to the superposition state of the atom via its stimulated interactions. The interference of the superposition state with itself reveals the encoded OPD. The de Broglie wave interferes with itself enabling measurement of the desired information encoded into it by the laser pulses.

As with optical interferometers, different atom interferometer configurations are used for different measurements. A variety of different atom interferometers configurations are being

considered for gravitational wave detection (see discussion in Section 2). For simplicity, this tutorial focuses on three-pulsed atom interferometry using the Raman process.

A.4. Raman Pulsed Atom Interferometry

$\frac{\pi}{2} - \pi - \frac{\pi}{2}$

In atom interferometry, beam splitting, mirroring, and combining are done through interactions of laser pulses with an atom. The beam splitting and beam combining pulses are the same type, $\frac{\pi}{2}$ laser pulses. Mirroring is done by a π laser pulse.

To understand the nature of these pulses and their name, the focus will be on a specific interaction of laser with an atom called *Raman process*. In this process, the relevant energy states of the atom are the ground state $|g\rangle$, excited state $|e\rangle$, and an intermediate state $|i\rangle$. If the initial state of the atom is the ground state $|g\rangle$, the desired state of the atom after applying the beam splitting $\frac{\pi}{2}$ pulse is the superposition state of $|g\rangle$ and $|e\rangle$. This state is represented by $|\psi\rangle$:

$$|\psi\rangle = C_1|g\rangle + C_2|e\rangle \quad \text{(E.5)}$$

Where C_1 and C_2 are complex coefficients. The physical interpretation of this atom state is that it is neither completely in the ground state nor in the excited state; the probability that the atom is in a ground state is $|C_1|^2$ and the probability that the atom is in an excited state is $|C_2|^2$. That is, a portion of the atom is in the ground state and a portion of it is in the excited state at the same time. If the atom initially is at the ground state $|g\rangle$, a portion of the atom, via stimulated absorption, absorbs the energy of the electromagnetic wave to be in excited state but it also absorbs the momentum and the phase of the electromagnetic wave. So, the portion of the atom in the excited state also has a different momentum and phase than the portion in the ground state.

Because different portions of the atom have different momentum, the implication of the atom being continuously in the superposition state is spatial separation after a finite time. This spatial separation increases the sensitivity to phase measurements, which will be discussed later in this document.

The phase of the laser also gets absorbed by the portion of the atom that is excited. This phase is added to the time evolution phase of the excited state portion of the superposition state. This phase is the desired information that is encoded to the atom by the laser. So, the above state becomes:

$$|\psi\rangle = C_1|g, \vec{p}_g\rangle + C_2 e^{i\varphi}|e, (\vec{p}_g + \vec{p}_{pulse})\rangle \quad \text{(E.6)}$$

where $\vec{p}_g$ is the momentum of the ground state and $\vec{p}_{pulse}$ is the momentum of the pulse. For a Raman process, $\vec{p}_{pulse}$ is equal to $2\hbar k$, where k is the wave vector of the laser.

If the atom initially starts in the excited state $|e\rangle$ with momentum $\vec{p}_g + \vec{p}_{pulse}$, a laser pulse can induce a transition back to the ground state $|g\rangle$ via stimulated emission. This interaction causes the state to evolve to

$$|\psi\rangle = C_2 e^{-i\varphi} |g, \vec{p}_g\rangle + C_1 |e, \vec{p}_g + \vec{p}_{pulse}\rangle \quad \text{(E.7)}$$

Note that unlike in Eq. (E.6), the phase of the ground state appears with a negative sign here. The component that makes the transition to the ground state picks up the phase factor and the change in momentum while the excited state remains unaffected. The key is interaction. The portion of the atom that interacts with the laser pulse gets the information and the other state is unaffected. The next section provides a detailed description of the C_1 and C_2 coefficients.

Figure A.2 represents a three-pulsed Raman atom interferometer Space-Time diagram. Pulses in this interferometer consist of two counter propagating lasers.

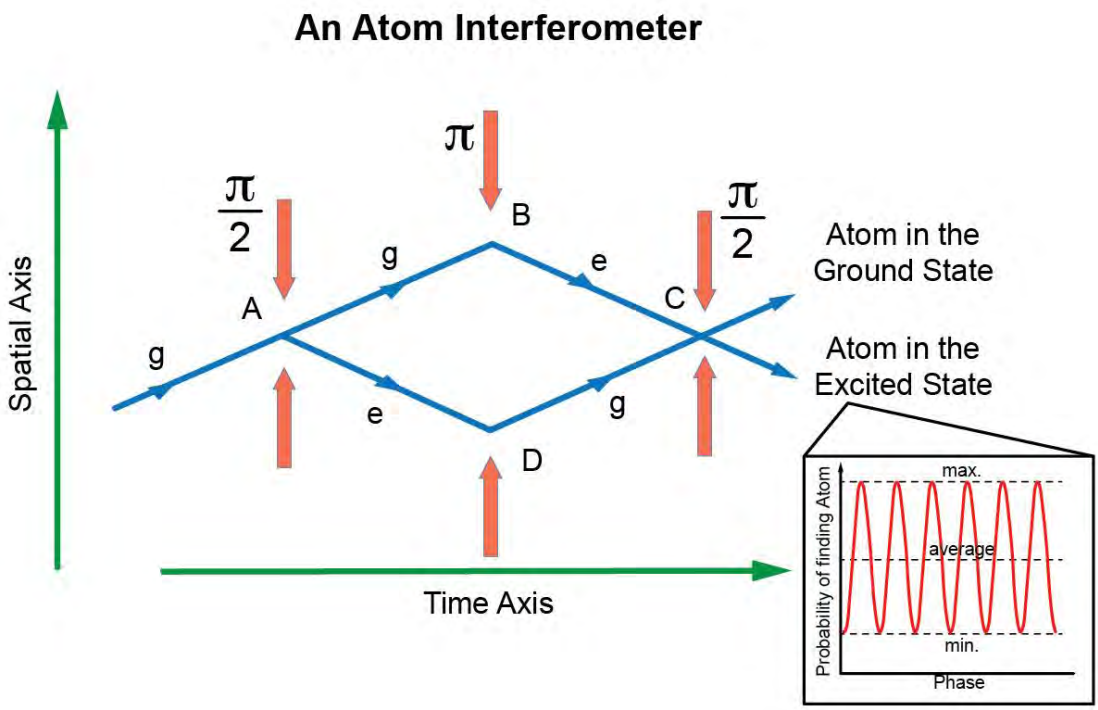

Figure A.2. A Three-Pulsed Raman Atom Interferometer

Figure A.2 is an analog to the Figure A.1 optical interferometer. Unlike the optical interferometer, which is a Space-Space diagram, the atom interferometer diagram is a Space-Time representation. An atom starts in the ground state and at time t_0 , a pulse of $\frac{\pi}{2}$ is applied to the atom. The pulse consists of two counter propagating laser pulses. Immediately after this pulse, the atom is in the superposition of the two states, with different momentum and phase. No other pulses are applied until the time $t_0 + T$. The above diagram depicts that, just before applying the second pulse, the states of the atom have been separated spatially due to the relative momentum (different slopes on the Space-Time diagram) between the two states.

Just like in an optical interferometer that splits the beam and uses mirrors to redirect them to spatially-overlap to create the fringes, the states of the atom also have to be redirected. Therefore, at time $t_0 + T$, a π pulse is applied that mirrors the components of the superposition state. This pulse reverses the momentum of the states and changes the ground state to the excited and the excited to the ground state. If the interferometer is ideal, at the time $t_0 + 2T$, the two states completely overlap and the final $\frac{\pi}{2}$ pulse is applied to recombine them.

The ground state appears at port one and the excited state appears at port two. As shown in Figure A.2, the two ports are spatially separated. The fringes in the atom interferometer are the probability of finding the atom in a specific state vs. the control provided by the phase of the final $\frac{\pi}{2}$ pulse.

Changing the phase of the final $\frac{\pi}{2}$ pulse acts like controlling the phase in optical interferometry using motion of the reference mirror. The phase difference between the two paths in this interferometer is expressed as,

$$\varphi_{ABC} - \varphi_{ADC} = \varphi = \varphi_3 - 2\varphi_2 + \varphi_1 \quad \text{(E.8)}$$

where φ_{ABC} and φ_{ADC} are phases of the different paths indicated in diagram.

$$\varphi_1 = (\varphi_{L_1} - \varphi_{L_2})_{t=t_0} \quad \text{(E.9)}$$

$$\varphi_2 = (\varphi_{L_1} - \varphi_{L_2})_{t=t_0+T} \quad \text{(E.10)}$$

$$\varphi_3 = (\varphi_{L_1} - \varphi_{L_2})_{t=t_0+2T} \quad \text{(E.11)}$$

φ_{L_1} and φ_{L_2} are the two laser phases at the time of interaction.

Probability of finding an atom in a ground state if the atom is initially in a ground state is:

$$P = \frac{1}{2}(1 + Cos\varphi) \quad \text{E.12}$$

The probability of finding an atom in an excited state if the atom is initially in the ground state is:

$$P = \frac{1}{2}(1 - Cos\varphi) \tag{E.13}$$

Just like with the fringes in optical interferometry, in atom interferometry, the probability of finding the atom in an excited state or the ground state are complimentary to each other and the summation of the two probabilities adds to one. This is equivalent of the conservation of energy in optical interferometry. The next section briefly covers interaction of the laser pulses with an atom and provides additional description of the $\frac{\pi}{2}$ and π pulses.

A.5. How do laser pulses interact with an atom?

As mentioned above, the Raman process involves three atomic levels called the ground state $|g\rangle$, excited state $|e\rangle$, and intermediate state $|i\rangle$. For appropriate choice of laser parameters [21], a two-photon transition occurs between states $|g\rangle$ and $|e\rangle$ via virtual transitions to the intermediate state $|i\rangle$. Since the intermediate state $|i\rangle$ remains essentially unpopulated during this process, the Raman transition can be described as an effective two level interaction between $|g\rangle$ and $|e\rangle$. Therefore for a Raman process we can accurately treat the atom as a two level system ($|g\rangle$ and $|e\rangle$) with energy states E_1 and E_2. In the absence of any external electromagnetic field, these are the eigenvalues of the unperturbed Hamiltonian.

When an external field is applied, an electric dipole moment is induced and the external field interacts with it. This adds a new term to the Hamiltonian of the system. If the electromagnetic field is polarized in the $\vec{x}$ direction, then the electron is displaced in the $\vec{x}$ direction with respect to the atom's center of mass. The dipole moment matrix element between the ground and excited states is d_{ge},

$$d_{ge} = -e\int \psi_g^* x\, \psi_e d^3r = -e\langle g|x|e\rangle \tag{E.14}$$

where ψ_g and ψ_e are the wave functions of the atom and the bracket is the Dirac notation for that integral. At any time, the wave function of the atom can be written as:

$$|\psi\rangle = C_1(t)|g\rangle e^{-iE_1t/\hbar} + C_2(t)|e\rangle e^{-iE_2t/\hbar} \tag{E.15}$$

Substituting this into the Schrodinger equation and taking advantage of the orthonormality of wave functions when integrating over space, the rate of change of $C_1(t)$ and $C_2(t)$ in time are described by the equation below:

$$\dot{C}_1(\mathrm{t}) = \mathrm{i}\frac{E_0 d_{ge}}{2\hbar}(e^{i(\omega-\omega_0)t} + e^{-i(\omega+\omega_0)t})\mathrm{C}_2(\mathrm{t}) \tag{E.16}$$

$$\dot{C}_2(\mathrm{t}) = \mathrm{i}\frac{E_0 d_{ge}}{2\hbar}(e^{-i(\omega-\omega_0)t} + e^{i(\omega+\omega_0)t})\,\mathrm{C}_1(\mathrm{t}) \quad \text{(E.17)}$$

where ω_0 is the resonant frequency of the two level atom:

$$\omega_0 = \frac{E_2 - E_1}{\hbar} \quad \text{(E.18)}$$

and the polarized external field is:

$$E_{ext} = (E_0, 0, 0)\,\mathrm{Cos}(\omega\,\mathrm{t}) \quad \text{(E.19)}$$

Introducing Rabi Frequency defined by:

$$\Omega_R = \left|\frac{d_{ge}E_0}{\hbar}\right| \quad \text{(E.20)}$$

the rate equations can be rewritten as:

$$\dot{C}_1(\mathrm{t}) = \mathrm{i}\frac{\Omega_R}{2}(e^{i(\omega-\omega_0)t} + e^{-i(\omega+\omega_0)t})\,\mathrm{C}_2(\mathrm{t}) \quad \text{(E.21)}$$

$$\dot{C}_2(\mathrm{t}) = \mathrm{i}\frac{\Omega_R}{2}(e^{-i(\omega-\omega_0)t} + e^{i(\omega+\omega_0)t})\,\mathrm{C}_1(\mathrm{t}) \quad \text{(E.22)}$$

A higher Rabi Frequency indicates a stronger laser and atom interaction. In atom interferometry, monochromatic power lasers are used and these interactions are strong. Assuming the resonant frequency of the atom, ω_0, and the frequency of the laser, ω, are the same, and neglecting the terms oscillating $\pm(\omega+\omega_0)$ and solving the equations above for $C_1(t)$ and $C_2(t)$:

$$C_1(\mathrm{t}) = \mathrm{Cos}(\Omega_R t/2) \quad \text{(E.23)}$$

$$C_2(\mathrm{t}) = i\,Sin(\Omega_R t/2) \quad \text{(E.24)}$$

Probabilities for finding the electron in the ground and excited states are then given by:

$$|C_1(\mathrm{t})|^2 = Cos^2(\Omega_R t/2) \quad \text{(E.25)}$$

$$|C_2(\mathrm{t})|^2 = Sin^2(\Omega_R t/2) \quad \text{(E.26)}$$

The time dependence of these probabilities shows that electron at time $t = \frac{\pi}{\Omega_R}$ is in the excited state, but at time $t = \frac{2\pi}{\Omega_R}$ is back to ground state. The process repeats itself with a period equal to $\frac{2\pi}{\Omega_R}$.

The atomic energy level oscillates back and forth between the ground and the excited states. This oscillatory behavior in response to the strong-field is called Rabi Oscillation or Rabi Flopping. If the external field (laser) is not at resonance with the atom, then the Rabi Frequency has the detuning term,

$$\Omega_{eff}{}^2 = \Omega_R{}^2 + (\omega - \omega_0)^2 \quad \text{(E.27)}$$

This shows the Rabi Frequency increases as the external field is detuned, but the probability of also finding the electron in the excited state is decreased by $(\frac{\Omega_R}{\Omega_{eff}})^2$,

$$|C_2(t)|^2 = (\frac{\Omega_R}{\Omega_{eff}})^2 Sin^2(\Omega_{eff} t / \hbar) \quad \text{(E.28)}$$

If there are no damping mechanisms, such as spontaneous emissions, then for a continuous external field, flopping continues until the field is turned off.

In atom interferometry, lasers are pulsed. So the electric field, E_0, is time varying. If E_0 is changing in time, so is the Rabi Frequency, Ω_R.

It is useful to define Pulse Area, Θ, according to:

$$\Theta = \left| \frac{d_{ge}}{\hbar} \int_{-\infty}^{\infty} E_0(t)\, dt \right| = \Omega_R t \quad \text{(E.29)}$$

A pulse that has an area of π is called π-pulse. An atom in the ground state will be in the excited state after interacting with a π-pulse. This atom remains excited until the spontaneous emission of the excited state. If shortly (i.e., in a shorter time than the lifetime of the electron in the excited state) after applying the π-pulse a 2π-pulse is applied, then the atom would transition to the ground state. For the same Rabi Frequency, a 2π-pulse is twice as long as a π-pulse. A $\frac{\pi}{2}$-pulse for the same Ω_R is half the length of a π-pulse.

A π-pulse makes a complete transition from the ground state to the excited state and vice versa. A $\frac{\pi}{2}$-pulse puts the atom in the superposition state. This is a state described by a coherent summation of the ground and excited state; there are specific phase relations between the two

states of this superposition state. Therefore, a portion of the atom is in the excited state and portion of it is in the ground state at the same time.

Figure A.2 demonstrates that the first $\frac{\pi}{2}$-pulse puts the atom that was initially in the ground state into superposition of the ground and excited state. After a time of T, free propagation for the states of the atom with different momentums, a π-pulse is applied. This pulse interacts with the superposition state and makes a transition from ground state to excited state and from excited state to ground state and reverses all momentums of the states' constituencies. After a time of T, the last $\frac{\pi}{2}$-pulse is applied. This pulse puts the ground state into superposition of the two states and also puts the excited state into superposition. The last pulse acts as combiner of the states. Then, the probability of detecting the atom in an excited and ground state is done in the ports of the atom interferometer.

A.6. Geometrical Interpretation of a Three Pulsed Atom Interferometer $\frac{\pi}{2}-\pi-\frac{\pi}{2}$

An arbitrary superposition state of a two level atom will have a wave function of the form given below:

$$|\psi\rangle = C_1|g\rangle + C_2|e\rangle \quad \text{(E.31)}$$

The normalization condition on the wave function requires that:

$$|C_1|^2 + |C_2|^2 = 1 \quad \text{(E.32)}$$

This suggests the state of the atom can be represented by a unit vector from the origin on a sphere. This vector is called the Bloch vector and the sphere is called a Bloch sphere. The direction of the Bloch vector can be represented in Cartesian or spherical coordinates. For a unit vector, they are related by,

$$\begin{aligned} x &= Sin\theta\ Cos\varphi \\ y &= Sin\theta\ Sin\varphi \\ z &= Cos\theta \end{aligned} \quad \text{(E. 33)}$$

Only two independent variables (θ, φ) are needed to define an arbitrary state of the atom.

The Bloch vector and the wave function can be connected by the top and bottom of the sphere to the ground and excited states respectively. The ground state, with $|\psi\rangle = |g\rangle$, thus corresponds to $(0,0,1)$ in the Cartesian and $(\theta = 0, \varphi = 0)$ in the spherical coordinate systems. The excited state,

with $|\psi\rangle = |e\rangle$ thus corresponds to $(0,0,-1)$ in Cartesian and $(\theta = \pi, \varphi = 0)$ in spherical coordinates. An arbitrary state in Cartesian coordinates is given by:

$$x = 2\,\mathrm{Re}(\mathrm{C}_1\, C_2)$$
$$y = 2\,\mathrm{Im}(\mathrm{C}_1\, C_2)$$
$$z = |C_2|^2 - |C_1|^2 \quad \text{(E.34)}$$

In polar coordinates, this simplifies to:

$$C_1 = Cos(\theta/2)$$
$$C_2 = e^{i\varphi}\, Sin(\theta/2) \quad \text{(E.35)}$$

with

$$0 \le \theta \le \pi$$
$$0 \le \varphi \le 2\pi \quad \text{(E.36)}$$

Therefore, the superposition state of an atom can be written in terms of the polar coordinates:

$$\psi = Cos(\theta/2)\ g + e^{i\varphi}\, Sin(\theta/2)\ e \quad \text{(E.37)}$$

This one-to-one mapping allows us to visualize an arbitrary superposition state of a two level atom in a geometric way, which is very useful when considering the resonant interaction with an intense laser.

Figure A.3 illustrates the states of the two level atom and its geometrical representation on the Bloch sphere. Every point on the sphere corresponds to a coherent state of a two level atom.

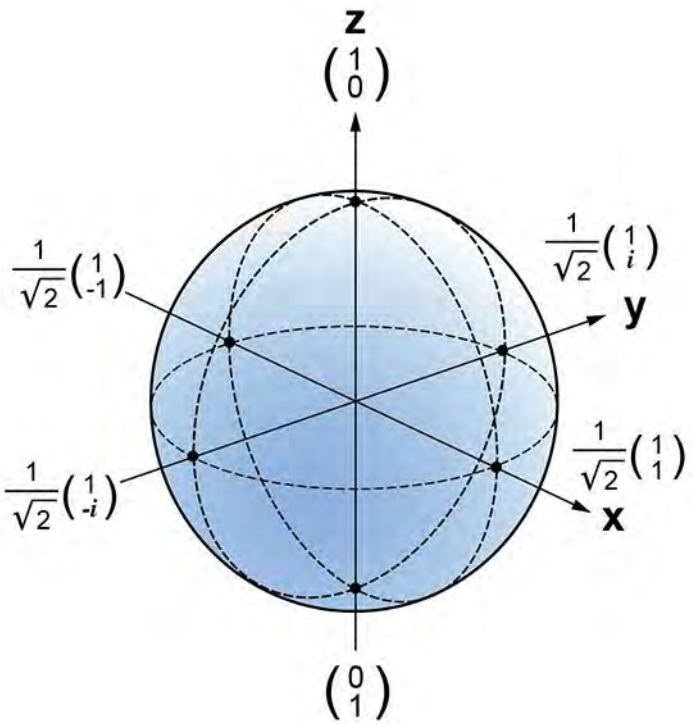

Figure A.3. The Bloch Sphere and States of an Atom

For example, the point on the positive x-axis is the state:

$$\frac{1}{\sqrt{2}}\begin{pmatrix}1\\1\end{pmatrix}=|\psi\rangle=Cos(\theta=\frac{\pi}{2}/2)|g\rangle+e^{i(\varphi=0)}Sin(\theta=\frac{\pi}{2}/2)|e\rangle=\frac{1}{\sqrt{2}}(|g\rangle+|e\rangle) \quad \text{(E.38)}$$

Likewise, the point on the x-axis on the negative side is:

$$\frac{1}{\sqrt{2}}\begin{pmatrix}1\\-1\end{pmatrix}=|\psi\rangle=Cos(\theta=\frac{\pi}{2}/2)|g\rangle+e^{i(\varphi=\pi)}Sin(\theta=\frac{\pi}{2}/2)|e\rangle=\frac{1}{\sqrt{2}}(|g\rangle-|e\rangle) \quad \text{(E.39)}$$

The time dependence of the wave function of a two level atom has an intrinsic angular frequency, ω_0 that is related to the energy difference between the two states via equation. The Bloch vector that represents the state of the atom rotates with an angular frequency of ω_0 about the Z-axis. If we make a coordinate transformation to this rotating frame, then the Bloch vector is stationary. Notice so far we have only assumed the bare atom and no external field. The question is what happens to the Bloch vector when the resonant external field is applied to the atom.

The application of a short resonant laser pulse is considered as a coherent operation on the Bloch vector. Assuming the damping time due to spontaneous emission is much longer than the pulse duration, then the magnitude of the Bloch vector is preserved and the Bloch vector only changes direction. This means the laser pulse acts as a rotation operator. A rotation operator acting on an initial Bloch vector results in another Bloch vector that can be acted upon by another rotation operator, and so on.

This process of applying rotational operators (laser pulses) to consecutive Bloch vectors can continue until the damping destroys the coherence of the superposition state of the atom. To represent the pulse lasers as rotation operators on the Bloch sphere, we use Pauli's rotation matrices. These rotational matrices are used for two-dimensional complex vector spaces more commonly than the more familiar three-dimensional rotational matrices used for a real three-dimensional vector space.

We do not make any attempt to derive them, but just list them and use them in this paper.

Rotation angle, θ, about the x, y, z axes can be performed using matrices below, respectively:

$$R_x(\theta)=\begin{pmatrix} Cos\frac{\theta}{2} & -i\,Sin\frac{\theta}{2} \\ -iSin\frac{\theta}{2} & Cos\frac{\theta}{2} \end{pmatrix} \quad \text{(E.40)}$$

$$R_y(\theta) = \begin{pmatrix} Cos\frac{\theta}{2} & -Sin\frac{\theta}{2} \\ -Sin\frac{\theta}{2} & Cos\frac{\theta}{2} \end{pmatrix} \quad \text{(E.41)}$$

$$R_z(\theta) = \begin{pmatrix} e^{-i\frac{\theta}{2}} & 0 \\ 0 & e^{i\frac{\theta}{2}} \end{pmatrix} \quad \text{(E.42)}$$

As previously discussed, starting with an atom in a ground state and applying a -pulse causes the atom to make a complete transition to the excited state. This can be examined using Bloch representation.

The atom in the ground state,

$$\begin{pmatrix} 1 \\ 0 \end{pmatrix} = |\psi\rangle = Cos(\theta = 0/2)\,|g\rangle + e^{i(\varphi=0)}\,Sin(\theta = 0/2)|e\rangle = |g\rangle \quad \text{(E.43)}$$

This vector points toward the positive $z$direction. Then, applying a rotation of $\theta = \pi$ about the x-axis to the Bloch vector $\begin{pmatrix} 1 \\ 0 \end{pmatrix}$:

$$R_x(\theta) = \begin{pmatrix} Cos\frac{\theta=\pi}{2} & -i\,Sin\frac{\theta=\pi}{2} \\ -iSin\frac{\theta=\pi}{2} & Cos\frac{\theta=\pi}{2} \end{pmatrix} = \begin{pmatrix} 0 & -i \\ -i & 0 \end{pmatrix} \quad \text{(E.44)}$$

$$|\psi\rangle = R_x(\pi)\,|g\rangle = \begin{pmatrix} 0 & -i \\ -i & 0 \end{pmatrix}\begin{pmatrix} 1 \\ 0 \end{pmatrix} = \begin{pmatrix} -i \\ 0 \end{pmatrix} = -i\begin{pmatrix} 0 \\ 1 \end{pmatrix} = -i\,|e\rangle \quad \text{(E.45)}$$

Except for an overall $-i$ phase, the atom is in the excited state. The Bloch vector points toward the - $z$direction. It is important to remember what the rotation operator physically represents. The laser pulse has intensity, polarization, and duration. The laser polarization induces an electric dipole in the atom in the direction of the polarization. This induced electric dipole interacts with the laser. The strength of this interaction is measured by Rabi Frequency, which is a product of the electric field of the laser and the magnitude of the induced dipole moment. The duration of the pulse multiplied by the Rabi Frequency generates the type of pulses, $\left(\pi, \frac{\pi}{2}, \frac{\pi}{3} \ldots\right)$, needed to transition the atom from one state to another. Next, consider the geometrical interpretation of a three-pulsed atom interferometer, starting with the ground state and applying successive

$\frac{\pi}{2} - \pi - \frac{\pi}{2}$ pulses about the x-axis. If ideal conditions are assumed (i.e., the phase of the laser pulses at the time of interaction are null), then after application of the three pulses the atom is at the ground state.

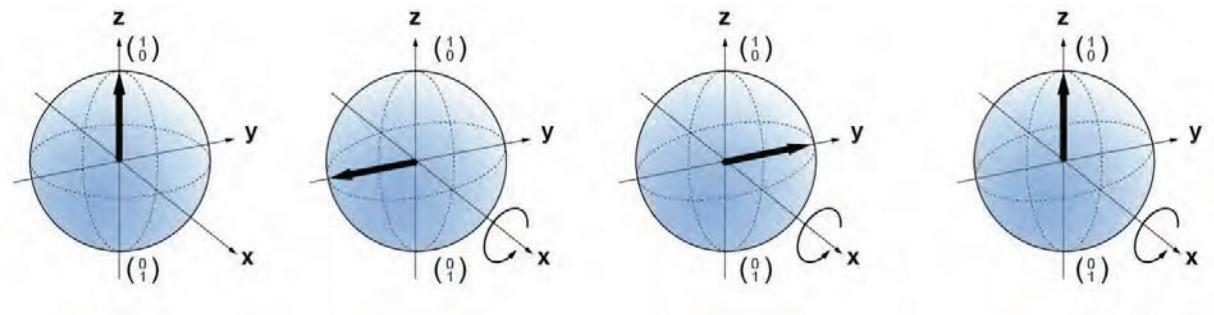

Figure A.4: The Three-Pulse Atom Interferometer

Figure A.4 depicts the successive application of these pulses to rotate the Bloch vector from initial state to final state. This can be calculated through the matrix multiplication below:

$$R_x(\frac{\pi}{2})R_x(\pi)R_x(\frac{\pi}{2})\,|g\rangle = \frac{1}{2}\begin{pmatrix} 1 & -i \\ -i & 1 \end{pmatrix}\begin{pmatrix} 0 & -i \\ -i & 0 \end{pmatrix}\begin{pmatrix} 1 & -i \\ -i & 1 \end{pmatrix}\begin{pmatrix} 1 \\ 0 \end{pmatrix} = -\begin{pmatrix} 1 \\ 0 \end{pmatrix} = +\,|g\rangle \quad \text{(E.46)}$$

Except for an overall phase, the atom is in the ground state. This shows the interpretation and formalism works, but what if at the time of application of the π-pulse the laser phase is not null.

In this case, the last $\frac{\pi}{2}$ pulse is applied with respect to the phase of the laser pulse that has been encoded to the component of the superposition state. That is, the $\frac{\pi}{2}$ rotation is done with respect to the Bloch vector that has the phase of the pulse laser after application of the π -pulse.

Figure A.5 displays the acquired phase before application of the final $\frac{\pi}{2}$ pulse. The state of the atom after the π-pulse with null laser phase is, $-\begin{pmatrix} 1 \\ i \end{pmatrix}$, and the state of the atom after the π -pulse with a laser phase of ϕ_L is $-\begin{pmatrix} e^{-i\phi_L} \\ ie^{+i\phi_L} \end{pmatrix}$. So, the ground state component of the superposition state picks up a phase factor of $e^{-i\phi_L}$ from the laser pulse. The excited state of the superposition state picks up a phase factor of $e^{+i\phi_L}$. The phase difference between the ground state and the excited state is $e^{+i2\phi_L}$. Now, applying the last $\frac{\pi}{2}$ pulse:

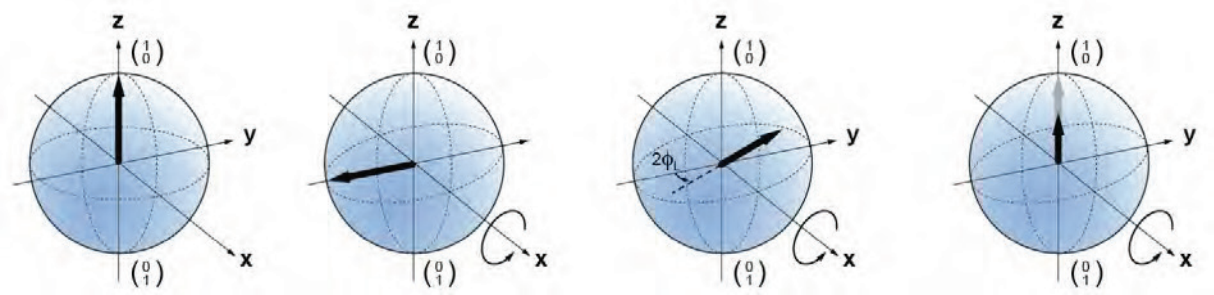

Figure A.5: The Three-Pulse Atom Interferometer with laser phase

$$\psi = -\frac{1}{2}\begin{pmatrix} 1 & -i \\ -i & 1 \end{pmatrix}\begin{pmatrix} e^{-i\phi_L} \\ ie^{+i\phi_L} \end{pmatrix} = -\frac{1}{2}\begin{pmatrix} e^{-i\phi_L} + e^{i\phi_L} \\ -i(e^{-i\phi_L} - e^{i\phi_L}) \end{pmatrix} = -\begin{pmatrix} Cos\phi_L \\ Sin\phi_L \end{pmatrix} = -(Cos\phi_L \ g + Sin\phi_L \ e)$$

So, the probability the atom is in the ground state is:

$$Cos\phi_L{}^2 = \frac{1}{2}(1 + Cos2\phi_L)$$

And the probability of finding the atom in the excited state is:

$$Sin\phi_L{}^2 = \frac{1}{2}(1 - Cos2\phi_L)$$

If the desired information to be detected is on the laser pulse, then this phase can be encoded to the states of the atom and detected through atom interferometry.

Bibliography

[1] Peter W. Graham, Jason M. Hogan, Mark A. Kasevich, and Surjeet Rajendran. New Method for Gravitational Wave Detection with Atomic Sensors. *Physical Review Letters*, 110(17):171102, April 2013.

[2] Savas Dimopoulos, Peter W. Graham, Jason M. Hogan, Mark A. Kasevich, and Surjeet Rajendran. Atomic gravitational wave interferometric sensor. *Physical Review D* , 78(12):122002, December 2008.

[3] Jason M. Hogan, David M. S. Johnson, Susannah Dickerson, Tim Kovachy, Alex Sugarbaker, Sheng-wey Chiow, Peter W. Graham, Mark A. Kasevich, Babak Saif, Surjeet Rajendran, Philippe Bouyer, Bernard D. Seery, Lee Feinberg, and Ritva Keski-Kuha. An atomic gravitational wave interferometric sensor in low earth orbit (AGIS-LEO). *General Relativity and Gravitation*, 43(7):1953–2009, May 2011.

[4] St Falke, H Schnatz, J S R Vellore Winfred, Th Middelmann, St Vogt, S Weyers, B Lipphardt, G Grosche, F Riehle, U Sterr, and Ch Lisdat. The 87 sr optical frequency standard at ptb. *Metrologia* , 48(5):399, 2011.

[5] D. S. Durfee, Y. K. Shaham, and M. A. Kasevich. Long-term stability of an area-reversible atom-interferometer sagnac gyroscope. *Phys. Rev. Lett.*, 97:240801, Dec 2006.

[6] R Geiger, V Ménoret, G Stern, N Zahzam, P Cheinet, B Battelier, A Villing, F Moron, M Lours, Y Bidel, A Bresson, A Landragin, and P Bouyer. Detecting inertial effects with airborne matter-wave interferometry. *Nature Communications*, 2:474, January 2011.

[7] M. J. Snadden, J. M. McGuirk, P. Bouyer, K. G. Haritos, and M. A. Kasevich. Measurement of the earth's gravity gradient with an atom interferometer-based gravity gradiometer. *Phys. Rev. Lett.*, 81:971–974, Aug 1998.

[8] Sheng-wey Chiow, Tim Kovachy, Hui-Chun Chien, and Mark A. Kasevich. 102hk Large Area Atom Interferometers. *Physical Review Letters*, 107(13):130403, September 2011.

[9] Jason M. Hogan, David M. S. Johnson, and Mark A. Kasevich. Light-pulse atom interferometry. In E. Arimondo, W. Ertmer, and W. P. Schleich, editors, *Proceedings of the International School of Physics "Enrico Fermi" on Atom Optics and Space Physics*, pages 411–447, Amsterdam, June 2009. IOS Press.

[10] Savas Dimopoulos, Peter W. Graham, Jason M. Hogan, and Mark A. Kasevich. Testing general relativity with atom interferometry. *Physical Review Letters*, 98:111102, Mar 2007.

[11] B.S. Sathyaprakash and Bernard F. Schutz. Physics, astrophysics and cosmology with gravitational waves. *Living Reviews in Relativity*, 12(2), 2009.

[12] B P Abbott and et al. Ligo: the laser interferometer gravitational-wave observatory. *Reports on Progress in Physics*, 72(7):076901, 2009.

[13] T Accadia and et al. Virgo: a laser interferometer to detect gravitational waves. *Journal of Instrumentation*, 7(03):P03012, 2012.

[14] J. M. McGuirk, G. T. Foster, J. B. Fixler, M. J. Snadden, and M. A. Kasevich. Sensitive absolute-gravity gradiometry using atom interferometry. *Physical Review A*, 65(3):033608, February 2002.

[15] J B Fixler, G T Foster, J M McGuirk, and M A Kasevich. Atom interferometer measurement of the newtonian constant of gravity. *Science*, 315(5808):74–7, January 2007.

[16] G. W. Biedermann. PhD thesis, Stanford University, 2008.

[17] John G. Baker and J. I. Thorpe. Comparison of atom interferometers and light interferometers as space-based gravitational wave detectors. *Phys. Rev. Lett.*, 108:211101, May 2012.

[18] Savas Dimopoulos, Peter W. Graham, Jason M. Hogan, and Mark A. Kasevich. General Relativistic Effects in Atom Interferometry. *Physical Review D* , 78(4):34, 2008.

[19] Ch.J. Bord. Atomic interferometry with internal state labelling. *Physics Letters A*, 140(12):10 – 12, 1989.

[20] F. Riehle, Th. Kisters, A. Witte, J. Helmcke, and Ch. J. Bordé. Optical ramsey spectroscopy in a rotating frame: Sagnac effect in a matter-wave interferometer. *Phys. Rev. Lett.*, 67:177–180, Jul 1991.

[21] Mark Kasevich and Steven Chu. Atomic interferometry using stimulated Raman transitions. *Physical Review Letters*, 67(2):181–184, July 1991.

[22] Savas Dimopoulos, Peter W. Graham, Jason M. Hogan, Mark A. Kasevich, and Surjeet Rajendran. Gravitational wave detection with atom interferometry. *Physics Letters B* , 678(1):37 – 40, 2009.

[23] Nan Yu and Massimo Tinto. Gravitational wave detection with single-laser atom interferometers. *General Relativity and Gravitation*, 43(7):1943–1952, 2011.

[24] M. Neugebauer, C. S. Wu, and J. D. Huba. Plasma fluctuations in the solar wind. *Journal of Geophysical Research: Space Physics*, 83(A3):1027–1034, 1978.

[25] P. Bender and et al. Lisa pre-phase a report.

[26] C. Antoine. Matter wave beam splitters in gravito-inertial and trapping potentials: generalized ttt scheme for atom interferometry. *Applied Physics B*, 84(4):585–597, 2006.

[27] Peter L. Bender. Comment on “atomic gravitational wave interferometric sensor”. *Phys. Rev. D*, 84:028101, Jul 2011.

[28] PeterL. Bender. Limitations of atom interferometry for gravitational wave observations in space. *General Relativity and Gravitation*, 44(3):711–717, 2012.

[29] Savas Dimopoulos, Peter W. Graham, Jason M. Hogan, Mark A. Kasevich, and Surjeet Rajendran. Reply to “comment on ‘atomic gravitational wave interferometric sensor’ ”. *Phys. Rev. D*, 84:028102, Jul 2011.

[30] G. T. Foster, J. B. Fixler, J. M. McGuirk, and M. A. Kasevich. Method of phase extraction between coupled atom interferometers using ellipse-specific fitting. *Optics Letters*, 27(11):951–953, 2002.

[31] G. Lamporesi, A. Bertoldi, L. Cacciapuoti, M. Prevedelli, and G. Tino. Determination of the Newtonian Gravitational Constant Using Atom Interferometry. *Physical Review Letters*, 100(5):050801, February 2008.

[32] Masao Takamoto and Hidetoshi Katori. Spectroscopy of the $^1s_0$-$^3p_0$ clock transition of ^{87}Sr in an optical lattice. *Phys. Rev. Lett.*, 91:223001, Nov 2003.

[33] St Falke, H Schnatz, J S R Vellore Winfred, Th Middelmann, St Vogt, S Weyers, B Lipphardt, G Grosche, F Riehle, U Sterr, and Ch Lisdat. The 87 sr optical frequency standard at ptb. *Metrologia* , 48(5):399, 2011.

[34] Rym Bouchendira, Pierre Claudé, Saïda Guellati-Khélifa, François Nez, and François Biraben. New Determination of the Fine Structure Constant and Test of the Quantum Electrodynamics. *Physical Review Letters*, 106(8):080801, February 2011.

[35] T. L. Gustavson, P. Bouyer, and M. A. Kasevich. Precision Rotation Measurements with an Atom Interferometer Gyroscope. *Physical Review Letters*, 78(11):2046–2049, March 1997.

[36] A. Peters, K. Y. Chung, and S. Chu. High-precision gravity measurements using atom interferometry. *Metrologia* , 38(1):25–61, February 2001.

[37] H. Müntinga, H. Ahlers, M. Krutzik, A. Wenzlawski, S. Arnold, D. Becker, K. Bongs, H. Dittus, H. Duncker, N. Gaaloul, C. Gherasim, E. Giese, C. Grzeschik, T. W. Hänsch, O. Hellmig, W. Herr, S. Herrmann, E. Kajari, S. Kleinert, C. Lämmerzahl, W. Lewoczko-Adamczyk, J. Malcolm, N. Meyer, R. Nolte, A. Peters, M. Popp, J. Reichel, A. Roura, J. Rudolph, M. Schiemangk, M. Schneider, S. T. Seidel, K. Sengstock, V. Tamma, T. Valenzuela, A. Vogel, R. Walser, T. Wendrich, P. Windpassinger, W. Zeller, T. van Zoest, W. Ertmer, W. P. Schleich, and E. M. Rasel. Interferometry with Bose-Einstein Condensates in Microgravity. *Physical Review Letters*, 110(9):093602, February 2013.

[38] See Supplemental Material at [URL TBD] for further description of Principal Component Analysis and its use in finding spatial fringe contrast.

[39] K. B. Davis, M. O. Mewes, M. R. Andrews, N. van Druten, D. Durfee, D. Kurn, and W. Ketterle. Bose-Einstein Condensation in a Gas of Sodium Atoms. *Physical Review Letters*, 75(22):3969–3973, November 1995.

[40] R. Dubessy, K. Merloti, L. Longchambon, P.-E. Pottie, T. Liennard, A. Perrin, V. Lorent, and H. Perrin. Rubidium-87 Bose-Einstein condensate in an optically plugged quadrupole trap. *Physical Review A*, 85(1):1–12, January 2012.

[41] Hubert Ammann and Nelson Christensen. Delta Kick Cooling: A New Method for Cooling Atoms. *Physical Review Letters*, 78(11):2088–2091, 1997.

[42] C. Monroe, W. Swann, H. Robinson, and C. Wieman. Very cold trapped atoms in a vapor cell. *Physical Review Letters*, 65(13):1571–1574, September 1990.

[43] J. Hecker Denschlag, J. E. Simsarian, H. Häffner, C. McKenzie, A. Browaeys, D. Cho, K. Helmerson, S. L. Rolston, and W. D. Phillips. A Bose-Einstein condensate in an optical lattice. *Journal of Physics B: Atomic, Molecular and Optical Physics* , 35(14):3095–3110, July 2002.

[44] Susannah Dickerson, Jason M. Hogan, David M. S. Johnson, Tim Kovachy, Alex Sugarbaker, Sheng-wey Chiow, and Mark A. Kasevich. A high-performance magnetic shield with large length-to-diameter ratio. *The Review of Scientific Instruments*, 83(6):065108, June 2012.

[45] Shau-Yu Lan, Pei-Chen Kuan, Brian Etsy, Phillipp Haslinger, and Holger M Müller. Influence of the Coriolis Force in Atom Interferometry. *Physical Review Letters*, 108(9):090402, February 2012.

[46] Stephen R. Segal, Quentin Diot, Eric A. Cornell, Alex A. Zozulya, and Dana Z. Anderson. Revealing buried information: Statistical processing techniques for ultracold-gas image analysis. *Physical Review A* , 81(5):053601, May 2010.

[47] Holger Müller, Sheng-wey Chiow, Sven Herrmann, Steven Chu, and Keng-Yeow Chung. Atom-Interferometry Tests of the Isotropy of Post-Newtonian Gravity. *Physical Review Letters*, 100(3):031101, January 2008.

[48] Jürgen Audretsch and Karl-Peter Marzlin. Ramsey fringes in atomic interferometry: Measurability of the influence of space-time curvature. *Physical Review A*, 50(3):2080–2095, September 1994.

[49] Paul R. Berman, editor. *Atom Interferometry.* Academic Press, San Diego, 1997.

[50] Michael A. Hohensee, Steven Chu, Achim Peters, and Holger Müller. Equivalence Principle and Gravitational Redshift. *Physical Review Letters*, 106(15):151102, April 2011.

[51] M Kasevich and S Chu. Measurement of the gravitational acceleration of an atom with a light-pulse atom interferometer. *Applied Physics B Photophysics and Laser Chemistry* , 54(5):321–332, May 1992.

[52] Susannah M Dickerson, Jason M Hogan, Alex Sugarbaker, David M S Johnson, and Mark A Kasevich. Multi-axis inertial sensing with long-time point source atom interferometry. 2013.

[53] The point source limit is relevant here only as an imaging artifact, resulting from $t_d > t_3$. The point source limit is not necessary for beam-tilt PSR.